AIMS Mathematics

AIMS Mathematics, 11(9): 29978–30011.
DOI: 10.3934/math.20261189
Received: 03 July 2026
Revised: 25 August 2026
Accepted: 08 September 2026
Published: 16 September 2026

http://www.aimspress.com/journal/Math

Research article

Thermal characteristics of (BNNTs+CdTe/RT42 HC) hybrid phase change nanofluid flow: Cooling electronic devices application

Mohammed H. Alharbi[1,*], Tarek G. Emam[2], and Essam M. Elsaid[3]

[1] Department of Mathematics and Statistics, College of Science, University of Jeddah, Jeddah, Saudi Arabia; mhhalharbi1@uj.edu.sa
[2] Department of Mathematics, Applied College, University of Jeddah, Jeddah, Saudi Arabia; temam@uj.edu.sa
[3] Basic Sciences Department, El Gazeera High institute for Engineering and Technology, Cairo, Egypt; essamscience@gmail.com

* **Correspondence:** Email: mhhalharbi1@uj.edu.sa.

Abstract: This study presents a numerical investigation of heat and mass transfer in a three-dimensional Williamson hybrid nanofluid composed of cadmium telluride (CdTe) and boron nitride nanotubes (BNNTs) dispersed in RT42 (Rubitherm), which is considered in its fully molten state. The flow is considered to be three-dimensional over a bidirectionally power-law stretching surface of variable thickness, including the effects of thermal radiation, internal heat generation, chemical reaction with activation energy, and Darcy–Forchheimer porous medium resistance. The governing nonlinear partial differential equations are transformed into a system of dimensionless ordinary differential equations using suitable similarity transformations, which, in turn, is solved numerically using shooting techniques through Mathematica functions NDSolve and FindRoot. The numerical method used is validated through comparing some obtained results with previously published limiting case results. The results show that increasing porous medium resistance suppresses fluid velocity while enhancing temperature and concentration distributions due to reduced convective transport. The increase of nanoparticle volume fractions increases the temperature profile and thermal-boundary-layer thickness; however, the accompanying decrease in the reduced Nusselt number indicates a reduction in the local wall heat-transfer rate. Increasing the radiation parameter from 0 to 2 decreased the reduced Nusselt number from 16.1657 to 8.3463, which corresponds to a reduction of approximately 48.4%. The reduced Nusselt number decreased from 17.4351 to 3.6625 upon increasing the Eckert number from 0 to 0.2, a reduction of approximately 78.9%. The primary wall-shear quantity rises by approximately 18.7% when the Forchheimer number increased from 0 to 2. The present study's main contribution is that it simultaneously treats Williamson rheology, BNNTs–CdTe/RT42 HC hybridization, non-Darcy porous resistance, thermal radiation, and Arrhenius kinetics within a single model. The results provide a theoretical basis for evaluating possible hybrid nanofluids in electronic thermal-management systems but not device-level validation.

Keywords: hybrid nanofluid; RT42 HC (Rubitherm); Williamson fluid; heat and mass transfer; Darcy–Forchheimer porous medium; Arrhenius activation energy
Mathematics Subject Classification: 76A05, 76S05, 80A20

1. Introduction

The goal of hybrid nanofluids (HNFs), which have emerged as an advanced class of engineered fluids, is to enhance the thermal performance of conventional heat transfer media. Such fluids are composed by the insertion of two or more types of nanofluids into some base fluid, which in turn improves the fluid thermophysical properties, such as thermal conductivity and energy transport. Such enhancement is due to the synergistic interaction between nanoparticles [1]. In comparison with traditional nanofluids, thin hybrid nanofluids have been confirmed through early studies to be efficient in applications of heat transfer, such as energy and industrial systems. Qureshi et al. demonstrated the efficiency of hybrid nanofluids in enhancing heat transfer efficiency and temperature control in the presence of magnetohydrodynamic conditions, proving their importance in advanced cooling technologies [2]. More recently, Norzawary et al. [3] compared hybrid carbon nanotube-based nanofluids with a single nanotube system and concluded that under slip and thermal radiation, the hybrid is better in heat transfer performance. Furthermore, Fatunmbi et al. [4] presented a study that expands this concept to include multi-hybrid nanofluids, and concluded that the addition of multiple nanoparticles significantly improves thermal efficiency in the presence of linear radiation and activation energy.

In addition, Akbar et al. [5] used an artificial neural network to investigate the model of heat transfer in hybrid and tri-hybrid nanofluids. They confirmed the effectiveness of such nanofluids in optimizing heat transfer in complex nonlinear systems.

New studies have shown that the makeup of nanoparticles and their rheological behaviour play a big role in controlling the movement of nanofluids. In [6], authors assessed how heat and mass move through bioconvective MHD nanofluids with different thermal properties. Other researchers [7,8] investigated the effects of nonlinear slip and hybrid nanoparticle combos, and others [9–11] investigated nanoparticle aggregation, rotation, thermal radiation, activation energy, and tri-hybrid nanoparticles. Also, [12] discussed how electrical conductivity and magnetization affect the flow of biomagnetic fluids that are full of particles.

The great interest shown in phase-change materials (PCMs) is justified, as they appear to be an effective solution for storing thermal energy due to their ability to absorb and release large amounts of latent heat during phase transformations, usually at a nearly constant temperature [13].

This unique characteristic of phase-change materials has made temperature regulation and energy efficiency enhancement possible in diverse applications, such as electronic device cooling, solar power systems, and battery temperature management. However, these materials inherently suffer from low thermal conductivity, which reduces their heat transfer rate and overall performance [14]. To address this deficiency, recent studies have focused on improving the properties of phase-change materials through making structural modifications and adding highly conductive materials, including nanoparticles and porous media. This has led to a significant enhancement in heat transfer efficiency [15].

Furthermore, significant improvements in thermal regulation and system efficiency can be seen through reduced operating temperatures and performance stabilization when phase-change materials are incorporated into advanced systems, such as photovoltaic modules [16]. It has been proven that nano-enhanced phase-change materials significantly improve thermophysical properties, including enhanced energy storage capacity and increased thermal conductivity, making them highly suitable for next-generation heat management applications.

RT42 HC (Rubitherm GmbH, Germany) has a suitable melting point of 42 °C and a high capacity for storing total latent heat; therefore, it is widely used in heat management applications and has proven particularly effective in regulating the temperature of power systems [17]. The ability of this material to absorb and release heat within a narrow temperature range makes it a valuable component used in lithium-ion battery cooling systems and solar thermal energy systems, but it is similar to traditional phase change materials PCMs in that it has low thermal conductivity, which negatively affects the rate of heat transfer and its overall efficiency [18]. This shortcoming has prompted researchers to conduct new studies aimed at improving thermal performance by adding conductive materials such as expanded graphite, and significant reductions in battery temperature and improvements in thermal stability have already been observed [19].

A significant improvement in modern heat management technologies has occurred when RT-series PMCs were successfully integrated into building and energy systems. This integration has led to an effective reduction in heat gain and an improvement in thermal resistance when incorporated into building materials. Moreover, a notable improvement in energy efficiency and temperature uniformity has occurred in advanced applications [20]. The property of shear thinning, where viscosity decreases as the shear rate increases, which characterizes non-Newtonian Williamson fluids, makes it more suitable for mixing complex liquids such as blood, polymers, and industrial suspensions [21]. Unlike Newtonian fluids, the non-linearity of the stress-strain relationships exhibited by these fluids significantly affects the heat transfer and flow characteristics in engineering systems. While early studies focused on analyzing the flow of Williamson nanofluid over expanding surfaces, demonstrating that the incorporation of nanoparticles improves thermal conductivity and enhances heat transfer performance under various physical conditions [22], subsequent studies have expanded to include thermal radiation, the fluid media, and the effects of magnetic fields. It has been observed that magnetohydrodynamic (MHD) forces tend to reduce flow velocity while improving temperature distribution and heat transfer behavior [23]. More recent studies have incorporated the effects of permeability, mixed convection, and thermal radiation, showing that parameters such as the Weissenberg number, thermal radiation, and porosity significantly influence fluid velocity and heat transfer rates in Williamson fluid systems [24]. Furthermore, advanced computational techniques, including artificial neural networks, have been introduced to model Williamson flux flow. This has provided more accurate predictions and improved analysis of nonlinear transport phenomena [25]. Furthermore, the important role played by thermal radiation and viscosity effects in controlling energy efficiency of Williamson fluid flows has been highlighted through thermodynamic analyses, such as irreversibility studies and entropy generation [26].

The role of heat and mass transfer processes is fundamental in some important engineering systems. These processes control energy transfer and fluid behavior through the coupled system of equations of conservation of mass, momentum, and energy. As for the advanced application of hydrogen storage, the interaction between heat and mass transfer is highly significant, since it influences system performance and reaction kinetics [27]. Recent studies have concluded that the optimization of flow configurations leads to enhancing heat and mass transfer rates and improves thermal uniformity [28]. Furthermore, macro-micro-modeling approaches have contributed to a deeper understanding of transport mechanisms and temperature distribution in complex systems [29]. In addition, controlling the transport efficiency is highly affected by multi-diffuse effects and fluid instability, which depends on Rayleigh and Reynolds numbers [30]. Studies have also showed that significant improvements in heat transfer are obtained by using enhancement techniques such as nanofluids [31]. Advanced numerical approaches have also been employed to investigate heat-transfer processes in nanostructured materials. Boundary-element formulations were developed for three-temperature transport in carbon-nanotube composites [32] and nanoparticle-assisted photothermal heat transfer [33]. These studies emphasize the importance of coupled transport mechanisms and advanced numerical modeling in thermal-management applications. In the Darcy-Forchheimer porous medium model, the effects of viscosity and inertia are incorporated to describe fluid flow and heat transfer in porous structures. This model has been widely used in modern studies. While Darcy's law is suitable for describing low-velocity flows, it suffers from a deficiency in capturing the effects of nonlinear inertia when the fluid velocity is high, which are modeled by the Forchheimer term in an effective way, leading to a more accurate non-Darcy model [34]. This model has important applications in energy systems, geothermal engineering, heat exchangers, and filtration processes. In these applications, transport phenomena are highly affected by porous medium [34]. According to recent studies, Darcy–Forchheimer parameters have a big effect on fluid velocity and temperature, as well as the concentration distribution. Such effect is crucial in nanofluid systems since it helps in reducing the velocity of the fluid while modifying thermal behavior [35].

Moreover, studies that incorporate magnetic fields and radiation effects and include hybrid and ternary nanofluids within Darcy–Forchheimer media found an enhancement of the heat transfer performance [36]. In addition, the coupling of Darcy–Forchheimer flow with activation energy and chemical reactions shows complex interactions that considerably influence heat and mass transfer rate [37].

Furthermore, the accuracy of modeling complex nanofluid flow systems is improved through c combining Darcy–Forchheimer effects with thermal radiation [38].

The term Arrhenius activation energy stands for the minimum energy required to initiate a chemical reaction. It has a very essential role in governing heat and mass transfer processes in reactive fluid systems [39]. The Arrhenius activation energy has significant influence on both of concentration distribution and reaction rates, which is particularly important in nanofluid flows through which chemical reactions and thermal effects are strongly coupled. Important applications, such as in chemical engineering, geothermal systems, and fluid mechanics, are highly benefited when the concept of Arrhenius activation energy is applied where reaction kinetics are described under varying thermal conditions.

Considering the activation energy is of great importance. A recent study showed that increasing the activation energy improves concentration distributions while reducing the effective reaction rate. This, in turn, leads to significant changes in the behavior of mass transfer [39]. Furthermore, the interaction between activation energy and thermal radiation has a major impact on the heat and mass selection characteristics of nanofluid systems, under magneto hydromagnetic conditions. In addition, the correlation of chemical reactions with Arrhenius activation energy in a study medium results in a complex nonlinear behavior that significantly affects velocity, temperature, and concentration domains. Moreover, advanced models incorporating activation energy, heating potential, and nanoparticle influence have demonstrated the accuracy of predicting transport phenomena in non-Newtonian nanofluid flows and surges [40]. In addition, combining Arrhenius activation energy with Darcy–

Forchheimer porous media and chemical reactions give rise to a complex nonlinear behavior. This behavior shows strong effects on velocity, temperature, and concentration fields [41].

Furthermore, an advanced model that combines activation energy, Joule heating, and nanoparticle effects is of great importance, as it allows improving the accuracy in predicting transport phenomena in non-Newtonian and hybrid nanofluid flows [42].

In fact, there is a need to further investigate the fields of hybrid nanofluids and porous media in a coupled way in one model to understand the coupling effect on transport phenomena; this is especially true for the synergistic interaction between Williamson non-Newtonian behavior, Darcy–Forchheimer inertial effects, and Arrhenius activation energy in the existence of thermal radiation.

This work seeks to fill this gap, providing a comprehensive model of heat and mass transfer in the flow of a Williamson-type hybrid nanofluid within a Darcy–Frochherimer-type porous medium. The study integrates the combined effects of radiation, activation energy, and hydromagnetic dynamics. The study comes close to embodying the complex interaction between rheology, porosity resistance, and chemical kinetics. This helps to obtain to give a deeper physical understanding and enhance the predictive capability of advanced systems of thermal management, providing a theoretical basis for evaluating possible hybrid nanofluids in electronic thermal-management systems, although not device-level validation.

2. Mathematical formulation

This study analyzes the continuous and constant flow of a hybrid nanofluid composed of cadmium telluride (CdTe) and boron nitride nanotubes (BNNTs) dispersed in RT42 (Rubitherm), which is considered in its fully molten state and maintained above its melting range. The nanofluid is considered both incompressible and viscous. The flow happens over a surface that extends in two opposite directions. The Williamson constitutive relation is employed to investigate the influence of shear-thinning behavior on the transport process. The Newtonian limit is recovered when the Weissenberg number satisfies $We = 0$. The effects of a chemical reaction as a thermal source are under consideration. In this case, we refer to the Cartesian coordinate system in which the x- and y-axes are coplanar with the extended surface, but the z-axis is orthogonal to the surface. The surface at $z = 0$ is elongated in the x- and y-directions with velocities $U_w = a(c + y + x)^n$ and $V_w = b(c + y + x)^n$, where a, b, c, and n are positive constants. The nonlinear stretching surface is maintained at the prescribed temperature $T_w(x, y)$, while the ambient fluid temperature is T_∞.

The effective properties of the fluid are evaluated sequentially by first dispersing CdTe nanoparticles in molten RT42 HC and then adding BNNTs to the resulting nanofluid. The same order is used consistently in the density, heat-capacity, viscosity, and thermal-conductivity relations. The adopted effective-medium relations assume uniform particle dispersion, low nanoparticle volume fractions, negligible particle aggregation, and negligible interfacial thermal resistance. The conductivity relation does not explicitly include the high aspect ratio or orientation of BNNTs. It is therefore used as an approximate effective-property model, and this limitation should be considered when interpreting the quantitative results. All thermophysical properties are evaluated at the melting range of RT42 HC, consistently with the fully molten assumption.

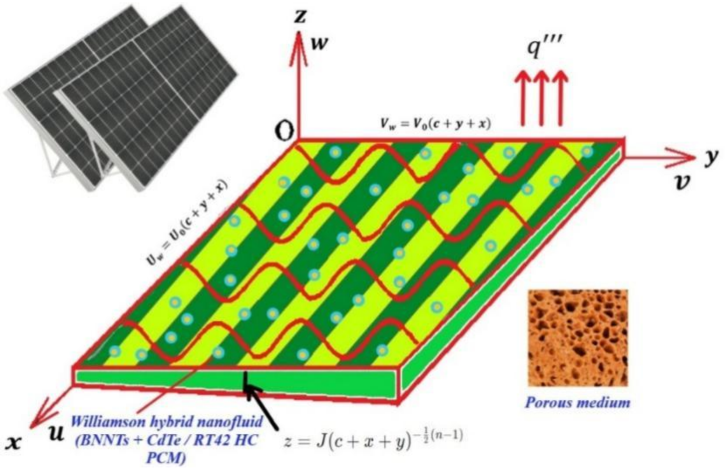

Figure 1. Geometric representation and dynamic coordinates.

The relevant governing boundary layer equations for the flow under consideration are given as follows [43–45]

$$\frac{\partial u}{\partial x}+\frac{\partial v}{\partial y}+\frac{\partial w}{\partial z}=0, \tag{1}$$

$$u\frac{\partial u}{\partial x}+v\frac{\partial u}{\partial y}+w\frac{\partial u}{\partial z}=\nu_{hnf}\frac{\partial^2 u}{\partial z^2}+\nu_{hnf}\frac{\Gamma}{\sqrt{2}}\frac{\partial}{\partial z}\left[\frac{\partial u}{\partial z}\sqrt{\left(\frac{\partial u}{\partial z}\right)^2+\left(\frac{\partial v}{\partial z}\right)^2}\right]-\frac{\nu_{hnf}}{K}u-\frac{C_F}{\sqrt{K}}|u|u, \tag{2}$$

$$u\frac{\partial v}{\partial x}+v\frac{\partial v}{\partial y}+w\frac{\partial v}{\partial z}=\nu_{hnf}\frac{\partial^2 v}{\partial z^2}+\nu_{hnf}\frac{\Gamma}{\sqrt{2}}\frac{\partial}{\partial z}\left[\frac{\partial v}{\partial z}\sqrt{\left(\frac{\partial u}{\partial z}\right)^2+\left(\frac{\partial v}{\partial z}\right)^2}\right]-\frac{\nu_{hnf}}{K}v-\frac{C_F}{\sqrt{K}}|v|v, \tag{3}$$

$$u\frac{\partial T}{\partial x}+v\frac{\partial T}{\partial y}+w\frac{\partial T}{\partial z}=\frac{k_{hnf}}{(\rho C_p)_{hnf}}\frac{\partial^2 T}{\partial z^2}+\frac{\mu_{hnf}}{(\rho C_p)_{hnf}}\left[1+\frac{\Gamma}{\sqrt{2}}\sqrt{\left(\frac{\partial u}{\partial z}\right)^2+\left(\frac{\partial v}{\partial z}\right)^2}\right]\left[\left(\frac{\partial u}{\partial z}\right)^2+\left(\frac{\partial v}{\partial z}\right)^2\right] \tag{4}$$

$$-\frac{1}{(\rho C_p)_{hnf}}\frac{\partial q_r}{\partial z}+\frac{1}{(\rho C_p)_{hnf}}q''',$$

$$q'''=\frac{k_{hnf}U_w}{\nu_{hnf}(c+x+y)}\left[A(T_w-T_\infty)u+B(T-T_\infty)\right],$$

$$u\frac{\partial C}{\partial x}+v\frac{\partial C}{\partial y}+w\frac{\partial C}{\partial z}=D_B\frac{\partial^2 C}{\partial z^2}-k_0(C-C_\infty)e^{-\frac{E_a}{R_0 T}}, \tag{5}$$

subjected to

$$\begin{cases} T=T_w, C=C_w, u=U_w, v=V_w, w=0, at\ z=J(c+y+x)^{-0.5(n-1)}, \\ T\to T_\infty, C\to C_\infty, u=v=0, at\ z\to z_\infty, \end{cases} \tag{6}$$

where,

$$U_w=a(c+y+x)^n, V_w=b(c+y+x)^n, C_w=C_0(x+y+c)^{0.5(1-n)}+C_\infty, T_w=T_0(c+y+x)^{0.5(1-n)}+T_\infty.$$

Equation (1) represents mass conservation. In Eqs (2) and (3), the left-hand sides describe convective momentum transport, whereas the right-hand sides represent viscous diffusion, Williamson non-Newtonian stress, and the linear Darcy and nonlinear Forchheimer resistances. In Eq (4), the terms denote thermal convection, conduction, viscous dissipation, radiative heat transfer, and internal heat generation. Equation (5) describes convective and diffusive species transport together with an Arrhenius chemical reaction. The boundary conditions (6) prescribe velocity, temperature, and concentration at the variable-thickness stretching surface and their free-stream values far from the surface.

The radiative heat flux under the Rosseland diffusion approximation is expressed as

$$q_r = -\frac{4\sigma^*}{3k^*}\frac{\partial T^4}{\partial z},$$

where σ^* is the Stefan-Boltzmann constant, and k^* is the mean absorption coefficient. For relatively small temperature differences, T^4 is expanded regarding the ambient temperature T_∞:$T^4 \approx 4T_\infty^3 T - 3T_\infty^4$. Higher-order terms are neglected.

Here, $V = (u, v, w)$ is the fluid velocity, $\Gamma > 0$ is the time constant, C and T are fluid concentration and temperature, respectively, ρ is the density, k is the thermal conductivity, C_p is heat capacitance, μ is the dynamic viscosity, and ν is the kinematic viscosity.

Table 1. Thermophysical properties of molten RT42 HC, CdTe nanoparticles, and BNNT nanoparticles [46–48].

Properties	RT42 HC	Cadmium telluride	Boron nitride
$\rho(kgm^{-3})$	760	5855	2100
$k(Wm^{-1}K^{-1})$	0.2	7.5	200
$C_p(Jkg^{-1}K^{-1})$	2000	209	1040
$\mu(Nsm^{-2})$	0.02351	-	-

The thermal and physical properties of hybrid nanofluids are given as follows [49]

$$\left.\begin{array}{c} \mu_{hnf} = \frac{\mu_f}{(1-\varphi_1)^{2.5}(1-\varphi_2)^{2.5}}, \\ \rho_{hnf} = (1-\varphi_2)\left[(1-\varphi_1)\rho_f + \varphi_1\rho_{p1}\right] + \varphi_2\rho_{p2}, \\ \left(\rho C_p\right)_{hnf} = (1-\varphi_2)\left[\left(\rho C_p\right)_f(1-\varphi_1) + \varphi_1\left(\rho C_p\right)_{p1}\right] + \varphi_2\left(\rho C_p\right)_{p2} \\ \frac{K_{bf}}{k_f} = \left(\frac{(k_{p1}+2\,k_f)-2\varphi_1(k_f-2k_{p1})}{(k_{p1}+2\,k_f)+\varphi_1(k_f-k_{p1})}\right) \\ \frac{K_{hnf}}{k_{bf}} = \left(\frac{(k_{p2}+2k_{bf})-2\varphi_2(k_{bf}-2k_{p2})}{(k_{p2}+2k_{bf})+\varphi_2(k_{bf}-k_{p2})}\right) \end{array}\right\}.$$

In this formulation, C represents s the concentration of a dilute dissolved reactive species undergoing molecular diffusion and an Arrhenius-type chemical reaction. While the nanoparticle volume fractions ϕ_1 and ϕ_2 are assumed to be uniform and constant throughout the flow domain, and their transport is not described by the concentration equation. A dilute-decoupling assumption is adopted.

Equation (4) becomes:

$$u\frac{\partial T}{\partial x}+v\frac{\partial T}{\partial y}+w\frac{\partial T}{\partial z}=\frac{k_{hnf}}{(\rho C_p)_{hnf}}\frac{\partial^2 T}{\partial z^2}+\frac{\mu_{hnf}}{(\rho C_p)_{hnf}}\left[1+\frac{\Gamma}{\sqrt{2}}\sqrt{\left(\frac{\partial u}{\partial z}\right)^2+\left(\frac{\partial v}{\partial z}\right)^2}\right]\left[\left(\frac{\partial u}{\partial z}\right)^2+\left(\frac{\partial v}{\partial z}\right)^2\right]-$$

$$\frac{1}{(\rho C_p)_{hnf}}\frac{\partial}{\partial z}\left(\frac{4\sigma}{3k^*}4T_\infty^3\frac{\partial T}{\partial z}\right)+\frac{1}{(\rho C_p)_{hnf}}\frac{k_{hnf}U_w}{\nu_{hnf}(c+x+y)}[A(T_w-T_\infty)u+B(T-T_\infty)].$$

In order to streamline our calculations, we have transformed the governing partial differential equations (PDEs) (2)–(5) and the corresponding boundary conditions (6) into non-linear ordinary differential equations (ODEs) using the prescribed transformation [44].

$$\xi=\left(\frac{(n+1)a}{2\nu_f}\right)^{\frac{1}{2}}(c+y+x)^{\frac{n-1}{2}}z,\psi=\left(\frac{2\nu_f a}{n+1}\right)^{\frac{1}{2}}F(\xi)(c+y+x)^{\frac{n+1}{2}},$$

$$u=F'(\xi)a(c+y+x)^n,v=H'(\xi)a(c+y+x)^n,\Theta(\eta)=\frac{T-T_\infty}{T_w-T_\infty},\Phi(\xi)=\frac{C-C_\infty}{C_w-C_\infty},$$

$$w=-\left(\frac{2\nu_f a}{n+1}\right)^{\frac{1}{2}}(c+y+x)^{\frac{n-1}{2}}\left[\left(H(\xi)+F(\xi)\right)\left(\frac{n+1}{2}\right)+\xi\left(H'(\xi)+F'(\xi)\right)\left(\frac{n-1}{2}\right)\right]. \tag{7}$$

By using (7), Eqs (2)–(5) reduce to

$$F'''+We\left[F'''\sqrt{F''^2+H''^2}+\frac{F''(F''F'''+H''H''')}{\sqrt{F''^2+H''^2}}\right] \tag{8}$$

$$-\frac{1}{A_1}\left[\frac{2n}{n+1}(F'+H')F'-(H+F)F''\right]-\frac{1}{D_a}F'-\frac{1}{A_1}F_rF'^2=0,$$

$$H'''+We\left[H'''\sqrt{F''^2+H''^2}+\frac{H''(F''F'''+H''H''')}{\sqrt{F''^2+H''^2}}\right] \tag{9}$$

$$-\frac{1}{A_1}\left[\frac{2n}{n+1}(F'+H')H'-(H+F)H''\right]-\frac{1}{D_a}H'-\frac{1}{A_1}F_rH'^2=0,$$

$$(1+Rd)\Theta''+\frac{PrA_3}{A_2}\left[\left(\frac{n-1}{n+1}\right)(F'+H')\Theta+(H+F)\Theta'\right] \tag{10}$$

$$+\frac{A_4}{A_2}PrEc\left[\left(F''^2+H''^2\right)+W_e\left(F''^2+H''^2\right)^{1.5}\right]+\frac{2}{n+1}\frac{1}{A_1}[AF'+B\Theta]=0,$$

$$\Phi''+Sc\left[\left(\frac{n-1}{n+1}\right)(F'+H')\Phi+(F+H)\Phi'\right]-\frac{2}{n+1}\gamma\, Sc\,\Phi\, e^{-\frac{\delta}{[1+\varepsilon\Theta]}}=0 \tag{11}$$

and the boundary condition (6) becomes:

$$F(\xi)=H(\xi)=\lambda\left(\frac{1-n}{1+n}\right),F'(\xi)=1,H'(\xi)=\alpha,\Theta(\xi)=\Phi(\xi)=1\ at\ \xi=\lambda,$$

$$F'(\xi)\to 0,H'(\xi)\to 0,\Theta(\xi)\to 0,\Phi(\xi)\to 0\ as\ \xi\to\infty. \tag{12}$$

In order to simplify calculations, it is necessary to convert the domain of the equations mentioned above, namely equations (8) to (12), from $[\lambda,\infty)$ to $[0,\infty)$. The new function is now:

$$\begin{cases} f(\eta)=F(\xi)=f(\xi-\lambda),h(\eta)=H(\xi)=h(\xi-\lambda),\\ \theta(\eta)=\Theta(\xi)=\theta(\xi-\lambda),\varphi(\eta)=\Phi(\xi)=\varphi(\xi-\lambda). \end{cases} \tag{13}$$

So, Eqs (8)–(11) become

$$f''' + We\left[f'''\sqrt{f''^2 + h''^2} + \frac{f''(f''f''' + h''h''')}{\sqrt{f''^2 + h''^2}}\right] \tag{14}$$
$$-\frac{1}{A_1}\left[\frac{2n}{n+1}(f' + h')f' - (h+f)f''\right] - \frac{1}{D_a}f' - \frac{1}{A_1}F_r f'^2 = 0,$$

$$h''' + We\left[h'''\sqrt{f''^2 + h''^2} + \frac{h''(f''f''' + h''h''')}{\sqrt{f''^2 + h''^2}}\right] \tag{15}$$
$$-\frac{1}{A_1}\left[\frac{2n}{n+1}(f' + h')h' - (h+f)h''\right] - \frac{1}{D_a}h' - \frac{1}{A_1}F_r h'^2 = 0,$$

$$(1 + Rd)\theta'' + \frac{PrA_3}{A_2}\left[\left(\frac{n-1}{n+1}\right)(f' + h')\theta + (h+f)\theta'\right] \tag{16}$$
$$+\frac{A_4}{A_2}PrEc\left[\left(f''^2 + h''^2\right) + W_e\left(f''^2 + h''^2\right)^{1.5}\right] + \frac{2}{n+1}\frac{1}{A_1}[Af' + B\theta] = 0,$$

$$\Omega'' + Sc\left[\left(\frac{n-1}{n+1}\right)(f' + h')\Phi + (f+h)\Omega'\right] - \frac{2}{n+1}\gamma\, Sc\, \Omega\, e^{-\frac{\delta}{[1+\varepsilon\theta]}} = 0 \tag{17}$$

and the boundary conditions are

$$f(0) = h(0) = \lambda\left(\frac{1-n}{1+n}\right), f'(0) = 1, h'(0) = \alpha, \tag{18}$$
$$\theta(0) = \Omega(0) = 1, f'(\infty) = h'(\infty) = 0, \theta(\infty) = \Omega(\infty) \to 0,$$

where

$$W_e = \frac{\Gamma}{\sqrt{2}}a(c+y+x)^{\frac{3n-1}{2}}\left(\frac{(1+n)a}{2\nu_f}\right)^{\frac{1}{2}}$$

is the Weissenberg number, α is the stretching ratio parameter, $Pr = \frac{(\mu C_p)_f}{k_f}$ is the Prandtl number, $Ec = \frac{a^2}{T_0(C_p)_f}(c+y+x)^{\frac{5n-1}{2}}$ is the Eckert number, $Rd = \frac{4\sigma T_\infty^3}{k^* k_f}$ is the radiation parameter, $Sc = \frac{\nu_f}{D_B}$ is the Schmidt number, $\lambda = J\left(\frac{(n+1)a}{2\nu_f}\right)^{\frac{1}{2}}$ is the wall thickness variable, $\gamma = k_0(x+y+c)^{(1-n)}$ is the chemical reaction parameter,

$$D = \frac{1}{D_a} = \frac{\nu_f}{KU_w}\frac{2}{n+1}(c+y+x)$$

is the inverse of the Darcy number, $F_r = \frac{C_F}{\sqrt{K}}\frac{2}{n+1}(c+y+x)$ is the Forchheimer number, $\delta = \frac{E_a}{R_0 T_\infty}$ is the activation energy parameter, $\varepsilon = \frac{(T_w - T_\infty)}{T_\infty}$ is (temperature-difference parameter in Arrhenius mode) the Arrhenius chemical constant, A is the temperature-reaction coupling coefficient, B is the thermal reaction parameter, and

$$A_1 = \frac{\nu_{hnf}}{\nu_f}, A_2 = \frac{k_{hnf}}{k_f}, A_3 = \frac{(\rho C_p)_{hnf}}{(\rho C_p)_f}, A_4 = \frac{\mu_{hnf}}{\mu_f}.$$

The transformation represents a local similarity formulation, in which the coordinate-dependent parameters are evaluated at a fixed surface location.

The local dimensionless skin friction coefficients for heat and mass transfer are:

$$C_{f_x} Re_x^{\frac{1}{2}} = 2\left(\frac{n+1}{2}\right)^{\frac{1}{2}} \left[1 + \{(f''(0))^2 + (h''(0))^2\}^{\frac{1}{2}} W\right] f''(0), \tag{19}$$

$$C_{f_y} Re_y^{\frac{1}{2}} = 2\alpha^{-\frac{3}{2}} \left(\frac{n+1}{2}\right)^{\frac{1}{2}} \left[1 + \{(f''(0))^2 + (h''(0))^2\}^{\frac{1}{2}} W_e\right] h''(0), \tag{20}$$

$$Nu_x Re_x^{-\frac{1}{2}} = -\left(\frac{n+1}{2}\right)^{\frac{1}{2}} \theta'(0), Sh_x Re_x^{-\frac{1}{2}} = -\left(\frac{n+1}{2}\right)^{\frac{1}{2}} \Omega'(0), \tag{21}$$

where $Re_x = \frac{(x+y+c)U_w}{\nu_f}$ is the local Reynolds number.

3. Proposed model solution and validation

The following auxiliary variables are used to transform the system of ODEs (14)–(18) is an uncoupled system of first order differential equations:

$$y_1 = f, y_2 = f', y_3 = f'', y_4 = h, y_5 = h', y_6 = h'',$$
$$y_7 = \theta, y_8 = \theta', y_9 = \Omega, y_{10} = \Omega'.$$

Using these definitions, the governing system together with the boundary conditions are written as follows:

$$y_1'(t) = y_2(t), y_2'(t) = y_3(t), \tag{22}$$

$$y_3'(t) = \frac{We\, y_3(t) y_6(t) P_5(t) - P_2(t)\left(R(t) + We\left(y_3(t)^2 + 2y_6(t)^2\right)\right)}{\left(1 + 2WeR(t)\right)\left(R(t) + We(y_3(t)^2 + y_6(t)^2)\right)}, \tag{23}$$

where

$$P_2(t) = -\frac{y_2(t)}{Da} - \frac{Fry_2(t)^2}{A_1} - \frac{-y_3(t)\left(y_1(t) + y_4(t)\right) + \frac{2ny_2(t)\left(y_2(t) + y_5(t)\right)}{1+n}}{A_1},$$

$$P_5(t) = -\frac{y_5(t)}{Da} - \frac{Fry_5(t)^2}{A_1} - \frac{\frac{2ny_5(t)\left(y_2(t) + y_5(t)\right)}{1+n} - \left(y_1(t) + y_4(t)\right)y_6(t)}{A_1},$$

$$y_4'(t) = y_5(t), y_5'(t) = y_6(t), \tag{24}$$

$$y_6'(t) = \frac{We\, y_3(t) y_6(t) P_2(t) - P_5(t)\left(R(t) + We\left(2y_3(t)^2 + y_6(t)^2\right)\right)}{\left(1 + 2WeR(t)\right)\left(R(t) + We(y_3(t)^2 + y_6(t)^2)\right)}, \tag{25}$$

$$y_7'(t) = y_8(t), \tag{26}$$

$$y_8'(t) = -\frac{1}{1+Rd}\left\{\frac{PrA_3}{A_2}\left[\frac{n-1}{n+1}\big(y_2(t)+y_5(t)\big)y_7(t)+\big(y_1(t)+y_4(t)\big)y_8(t)\right]+\frac{A_4}{A_2}PrEc\left[y_3(t)^2+y_6(t)^2+We\left(y_3(t)^2+y_6(t)^2\right)^{\frac{3}{2}}\right]+\frac{2}{(n+1)A_1}\left[A\,y_2(t)+B\,y_7(t)\right]\right\}, \quad (27)$$

$$y_9'(t) = y_{10}(t), \quad (28)$$

$$y_{10}'(t) = -\frac{n-1}{n+1}Sc\left(y_2(t)+y_5(t)\right)y_7(t) - Sc\left(y_1(t)+y_4(t)\right)y_{10}(t)+\frac{2}{1+n}Sc\,\gamma\,y_9(t)E(t) \quad (29)$$

where $E(t) = \exp\left(-\frac{\delta}{1+\varepsilon\,y_7(t)}\right)$.

The initial conditions are:

$$y_1(0) = \frac{\lambda(1-n)}{n+1},\ y_2(0)=1,\ y_3(0)=s_1,\ y_4(0)=\frac{\lambda(1-n)}{n+1},\ y_5(0)=\alpha, \quad (30)$$
$$y_6(0)=s_2,\ y_7(0)=1,\ y_8(0)=s_3,\ y_9(0)=1,\ y_{10}(0)=s_4.$$

The shooting technique, combined with the functions *NDSolve* and *FindRoot* in *Mathematica* is used to solve the system since there are missing initial values, namely s_1, s_2, s_3, and s_4. First, effective nanofluid properties, such as ρ_{nf}, μ_{nf}, k_{nf}, $\left(\rho C_p\right)_{nf}$, and σ_{nf}, are by introducing the thermophysical properties of the base fluid and the nanoparticles, together with the prescribed nanoparticle volume fractions. Such quantities are used to calculate the derived coefficients A_1–A_4, appearing in the transformed differential equations. The resulting system is written in compact form as follows:

$$\mathbf{Y}'(\eta) = \mathbf{F}(\eta,\mathbf{Y};M,Pr,Sc,\lambda,\gamma,\ldots), \quad \mathbf{Y} = [y_1,y_2,\ldots,y_{10}]^T.$$

Since there are unknown shooting parameters,

$$s_1 = f''(0), \qquad s_2 = h''(0), \qquad s_3 = \theta'(0), \qquad s_4 = \Omega'(0),$$

the initial-condition vector is written as, $\mathbf{Y}(0) = [f(0), f'(0), s_1, h(0), h'(0), s_2, \theta(0), s_3, \Omega(0), s_4]^T$, where the remaining entries are known from the wall boundary conditions. The interval of solution is truncated at a selected sufficiently large η_∞, which satisfies the asymptote boundary conditions. In these calculations, the maximum value η_∞ of is 6. Suitable guessing values of the shooting parameters are assigned; then, using the shooting vector $\mathbf{s} = [s_1,s_2,s_3,s_4]^T$,the initial-value problem is integrated from $\eta = 0$ to $\eta = \eta_\infty$ using *NDSolve*. To improve robustness when the equations become stiff for certain parameter combinations, the integration is carried out using Method ->"Stiffness Switching".

Once the trial integration is performed, the residual vector is calculated, which is defined as

$$\mathbf{R}(\mathbf{s}) = \begin{bmatrix} f'(\eta_\infty) - f'_\infty \\ h'(\eta_\infty) - h'_\infty \\ \theta(\eta_\infty) - \theta_\infty \\ \Omega(\eta_\infty) - \Omega_\infty \end{bmatrix}.$$

Since the far-field values are zero, $\mathbf{R}(\mathbf{s})$ reduces to

$$\mathbf{R}(\mathbf{s}) = \begin{bmatrix} f'(\eta_\infty) \\ h'(\eta_\infty) \\ \theta(\eta_\infty) \\ \Omega(\eta_\infty) \end{bmatrix}.$$

$\mathbf{R}(\mathbf{s})$ is aimed to satisfy: $\mathbf{R}(\mathbf{s}) = \mathbf{0}$.

The algebraic equations are then solved simultaneously using *Mathematica* function *FindRoot*. The suitable assumed values of s_1^{guess}, s_2^{guess}, s_3^{guess}, and s_4^{guess} are considered as initial values. *FindRoot* repeatedly calls the shooting function. The *Mathematica* function NDSolve reintegrates the first-order system for every iteration and hence, the far-field residuals are recalculated to correct estimates of the shooting parameters. The iteration is terminated when $\max_{1 \le i \le 4} |R_i| < \varepsilon_R$, where ε_R is the prescribed residual tolerance, which is assigned in these calculations as 10^{-6}. The resulting converged values, denoted by $s_1^{sol}, s_2^{sol}, s_3^{sol}, s_4^{sol}$, are then substituted into the initial conditions, and the system is integrated once more to generate the final continuous solution over $0 \le \eta \le \eta_\infty$. The values of $s_1^{sol}, s_2^{sol}, s_3^{sol}, s_4^{sol}$, obtained at a single parameter value, are then used as initial guesses for the next neighboring value of this parameter, in order to improve numerical stability and reduce the computational effort. The profiles of velocity, secondary-velocity, temperature, and concentration $f'(\eta), h'(\eta), \theta(\eta), \Omega(\eta)$ are then constructed using the converged numerical solution sampled on a sufficiently fine set of points, while the wall transport quantities are calculated directly from the converged shooting parameters.

The method of solving system (22)–(28) is shown in the flow chart in Figure 2.

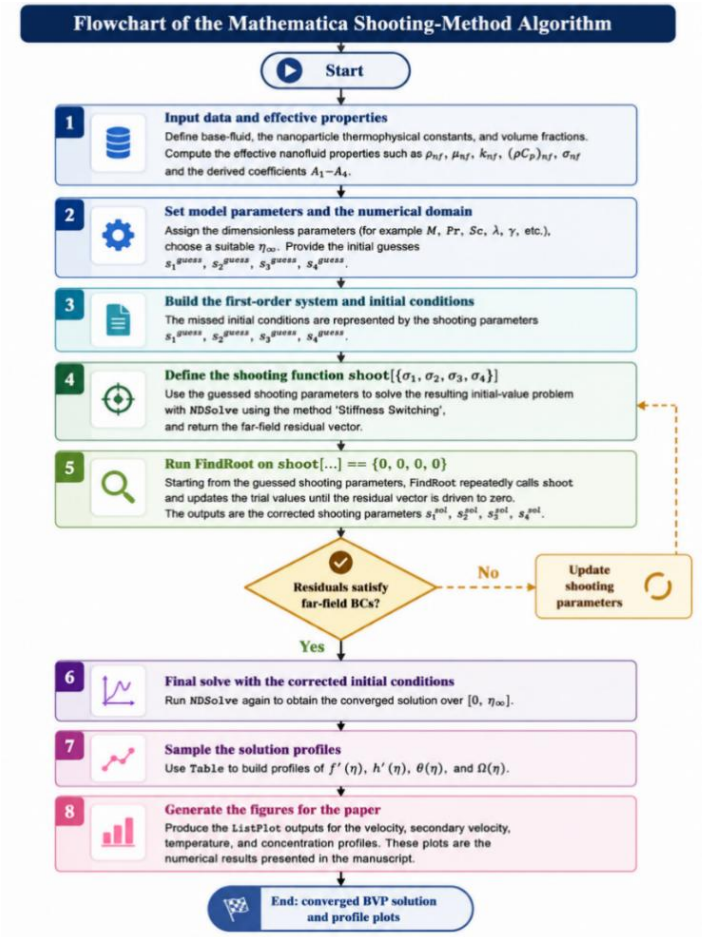

Figure 2. Flow diagram for the solution.

To validate the method used in this paper, a comparison of the present numerical solution with the HAM results reported by Hayat et al [50] is given for some limiting cases of skin friction. The comparison shows excellent agreement, confirming the reliability of the present method.

Table 2. Skin friction comparison with earlier findings.

	α	$-\sqrt{Re_x}\,C_{fx}$		$-\sqrt{Re_x}\,C_{fy}$	
		$n = 1$	$n = 1.5$	$n = 1$	$n = 1.5$
Hayat et al. [50] HAM-method		1.0954	1.3002	2.4495	2.9073
Al Qarni [51]	0.2	1.0954	1.3002	2.4495	2.9075
Present results Numerical method		1.0954	1.3002	2.4495	2.9073

4. Outcomes interpretation

This study aims to examine the flow of a single-phase Williamson hybridized nanofluid, with RT42 HC (Rubitherm) as a base fluid, which is a change phase material (PCM). Two kinds of nanoparticles are dispersed on the nanofluid, i.e., cadmium telluride (CdTe) and boron nitride nanotubes (BNNTs). Also, a set of diverse parameter effects are considered, the most important of which in this study is the thermal radiation parameter. The following effects are also studied: the power index, wall thickness variable, and stretchable ratio parameter, on both the horizontal and vertical velocities, temperature, and concentration outlines. Moreover, the Eckert number and the heat source parameter on the temperature file are also studied. The consequences of the chemical reaction are also discussed on the concentration profile. We used the appropriate numerical method, the shooting numerical method with FindRoot methodology, to study the different and potential effects of the parameters that govern this problem. Figures 3–21 and Table 3 examine the different effects on each of the horizontal and vertical velocities profiles, temperature, and concentration outlines, as well as surface frictional force, heat, and mass transfers. When performing numerical calculations, the values of the parameters are fixed at the following values: $\boldsymbol{\varphi_1 = 0.01, \varphi_2 = 0.01, We = 0.2, n = 0.7}$, $\boldsymbol{\lambda = 0.2}$, $\boldsymbol{\alpha = 0.8}$, $\boldsymbol{Rd = 1}$, $\boldsymbol{D = 1}$, $\boldsymbol{Ec = 0.1}$, $\boldsymbol{Sc = 1}$, $\boldsymbol{Fr = 1}$, $\boldsymbol{\gamma = 1, A = 0.1}$, $\boldsymbol{B = 0.1}$, $\boldsymbol{\varepsilon = 0.2}$, $\boldsymbol{\delta = 1}$; only the value of the parameter under study is changed.

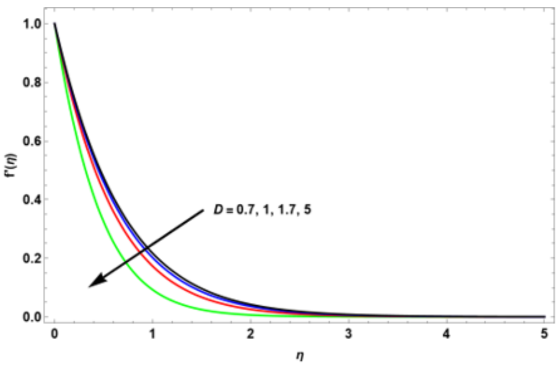

Figure 3. Behavior of $\boldsymbol{x}$ −velocity versus change D.

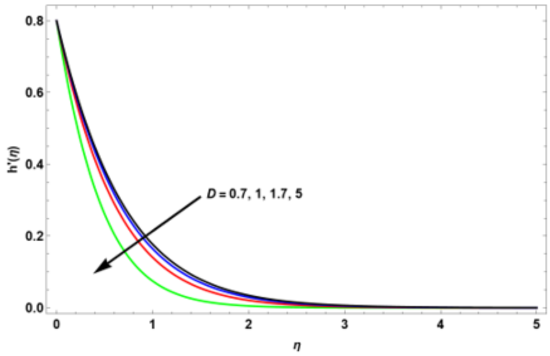

Figure 4. Behavior of y −velocity versus change in D.

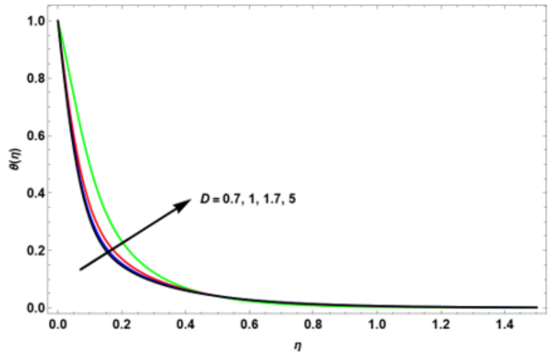

Figure 5. Behavior of temperature versus change in D.

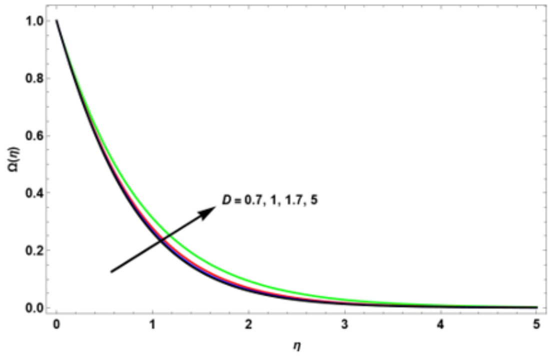

Figure 6. Behavior of temperature versus change in D.

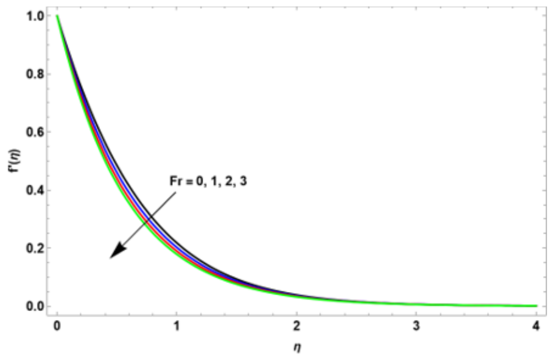

Figure 7. Behavior of x −velocity versus change in Fr.

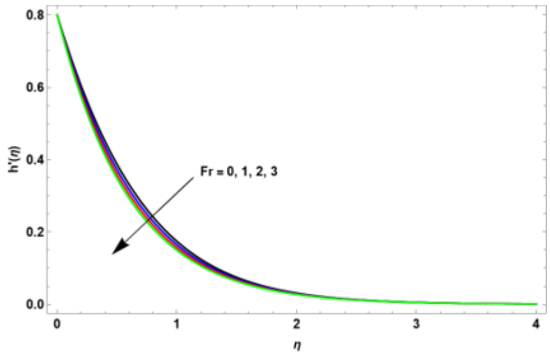

Figure 8. Behavior of y −velocity versus change in Fr.

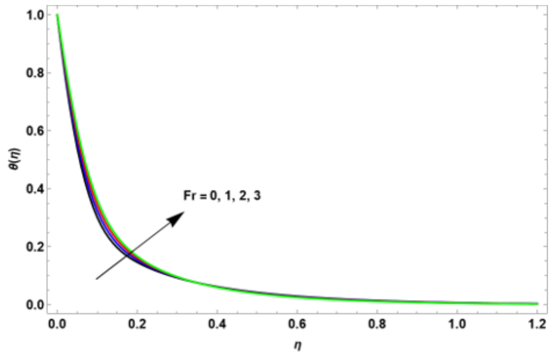

Figure 9. Behavior of temperature versus change in Fr.

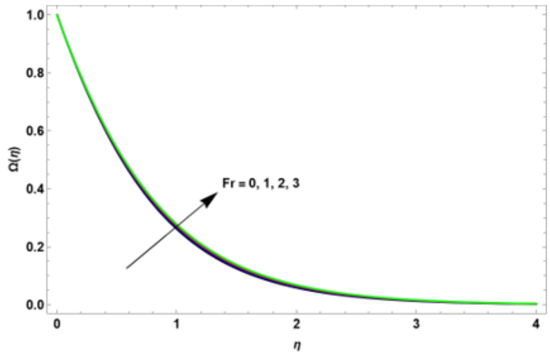

Figure 10. Behavior of concentration versus change in Fr.

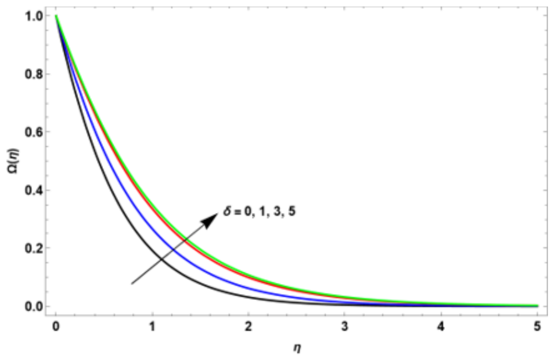

Figure 11. Behavior of concentration versus change in δ.

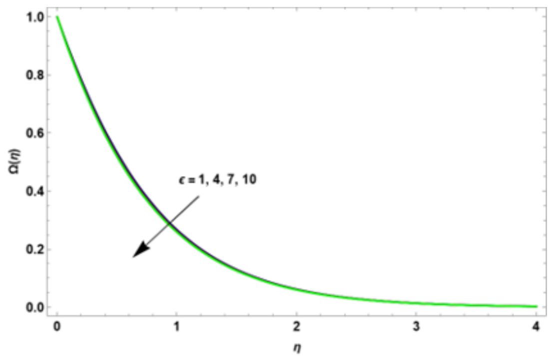

Figure 12. Behavior of concentration versus change in ε.

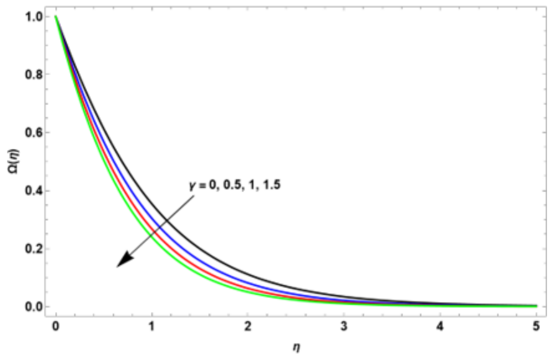

Figure 13. Behavior of concentration versus change in n γ.

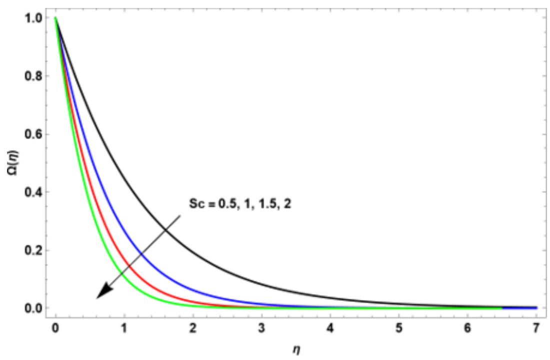

Figure 14. Behavior of concentration versus change in Sc.

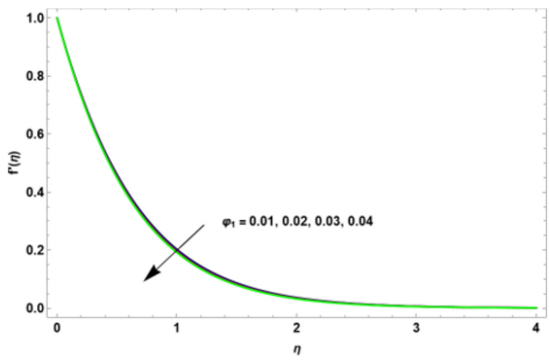

Figure 15. Behavior of x −velocity versus change in φ_1.

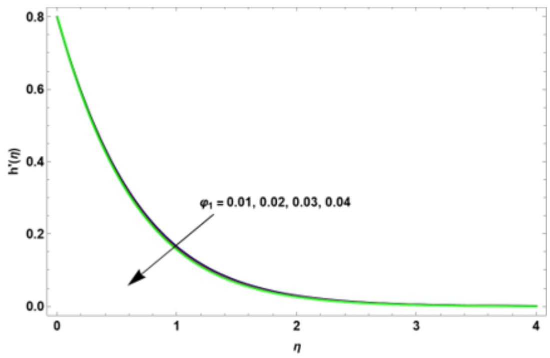

Figure 16. Behavior of y−velocity versus change in φ_1.

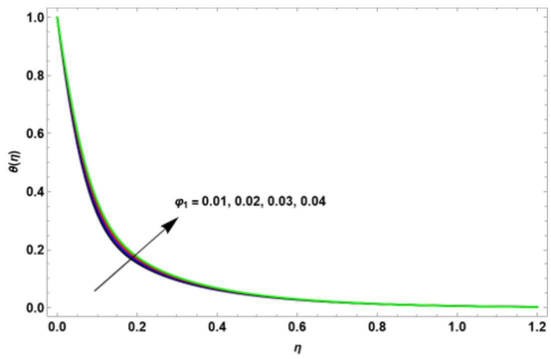

Figure 17. Behavior of temperature versus change in φ_1.

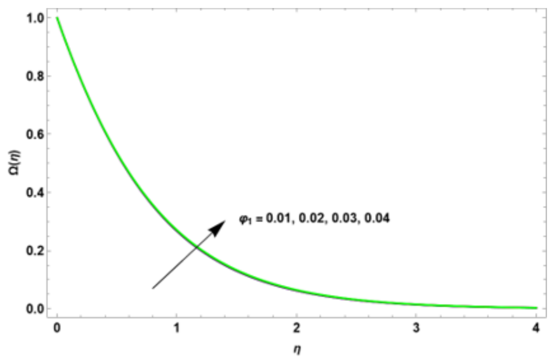

Figure 18. Behavior of concentration versus change in φ_1.

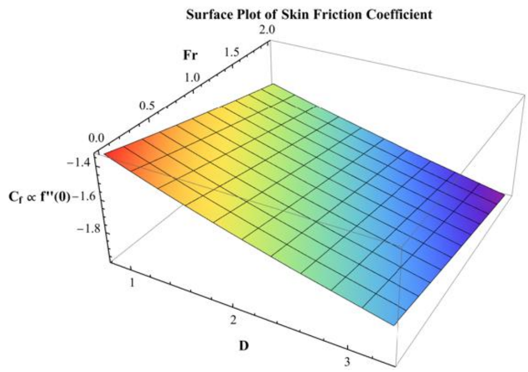

Figure 19. Behavior of skin friction versus change in Fr & D.

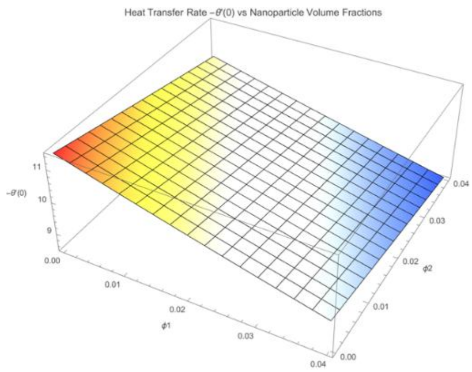

Figure 20. Behavior of Nusselt number versus change in φ_1& φ_2.

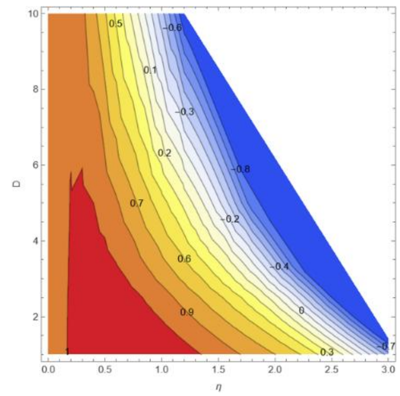

Figure 21. Contour map of temperature versus change in D.

Table 3. Effects of variation of the controlling parameters on $-f''(0)$, $-h''(0)$, $-\theta'(0)$, and $-\Omega'(0)$.

A	B	D	δ	Ec	ε	Fr	γ	φ_1	φ_2	Rd	Sc	$-f''(0)$	$-h''(0)$	$-\theta'(0)$	$-\Omega'(0)$
0.1												1.502201	1.175421	10.548769	1.177527
0.5												1.502201	1.175421	10.509244	1.177667
1	0.1	1.0	1.0	0.1	1.0	1.0	1.0	0.01	0.01	1.0	1.0	1.502201	1.175421	10.459838	1.177842
1.5												1.502201	1.175421	10.410431	1.178016
2												1.502201	1.175421	10.361025	1.178191
	0.1											1.502201	1.175421	10.548769	1.177527
	0.5											1.502201	1.175421	10.534627	1.177544
0.1	**1**	1.0	1.0	0.1	1.0	1.0	1.0	0.01	0.01	1.0	1.0	1.502201	1.175421	10.516927	1.177565
	1.5											1.502201	1.175421	10.499203	1.177586
	2											1.502201	1.175421	10.481455	1.177607
		0.4										1.379686	1.073901	11.610495	1.194647
		0.5										1.401210	1.091797	11.429187	1.191572
0.1	0.1	0.7	1.0	0.1	1.0	1.0	1.0	0.01	0.01	1.0	1.0	1.436040	1.120698	11.131085	1.186658
		1.0										1.502201	1.175421	10.548769	1.177527
		2.0										1.678644	1.320487	8.892590	1.154469
0.1	0.1	1.0	**0**	0.1	1.0	1.0	1.0	0.01	0.01	1.0	1.0	1.502201	1.175421	10.548769	1.462944
			0.5									1.502201	1.175421	10.548769	1.300051

Continued on next page

A	B	D	δ	Ec	ε	Fr	γ	φ_1	φ_2	Rd	Sc	$-f''(0)$	$-h''(0)$	$-\theta'(0)$	$-\Omega'(0)$
			1									1.502201	1.175421	10.548769	1.177527
			1.5									1.502201	1.175421	10.548770	1.088410
			2									1.502201	1.175421	10.548770	1.025586
				0.00								1.502201	1.175421	17.435056	1.161165
				0.05								1.502201	1.175421	13.991913	1.169670
0.1	0.1	1.0	1.0	**0.10**	1.0	1.0	1.0	0.01	0.01	1.0	1.0	1.502201	1.175421	10.548769	1.177527
				0.15								1.502201	1.175421	7.105626	1.184806
				0.2								1.502201	1.175421	3.662482	1.191570
					0.5							1.502201	1.175421	10.548769	1.164066
					1							1.502201	1.175421	10.548769	1.177527
0.1	0.1	1.0	1.0	0.1	**2**	1.0	1.0	0.01	0.01	1.0	1.0	1.502201	1.175421	10.548769	1.198437
					3							1.502201	1.175421	10.548769	1.214389
					4							1.502201	1.175421	10.548769	1.227255
						0						1.366643	1.093314	11.386216	1.188115
						0.5						1.436582	1.135328	10.963096	1.182631
0.1	0.1	1.0	1.0	0.1	1.0	**1**	1.0	0.01	0.01	1.0	1.0	1.502201	1.175421	10.548769	1.177527
						1.5						1.564115	1.213781	10.142563	1.172752
						2.0						1.622809	1.250573	9.743885	1.168266
							0					1.502201	1.175421	10.548770	0.895643
							0.5					1.502201	1.175421	10.548770	1.047733
0.1	0.1	1.0	1.0	0.1	1.0	1.0	**1**	0.01	0.01	1.0	1.0	1.502201	1.175421	10.548769	1.177527
							1.5					1.502201	1.175421	10.548769	1.293289
							2					1.502201	1.175421	10.548769	1.399098
								0				1.484020	1.161523	11.076745	1.179272
								0.01				1.502201	1.175421	10.548769	1.177527
0.1	0.1	1.0	1.0	0.1	1.0	1.0	1.0	**0.02**	0.01	1.0	1.0	1.518821	1.188130	10.038789	1.176010
								0.03				1.533977	1.199724	9.545749	1.174706
								0.04				1.547757	1.210267	9.068670	1.173601
									0			1.518643	1.187994	10.906175	1.174730
									0.01			1.502201	1.175421	10.548769	1.177527
0.1	0.1	1.0	1.0	0.1	1.0	1.0	1.0	0.01	**0.02**	1.0	1.0	1.485934	1.162985	10.201642	1.180321
									0.03			1.469844	1.150689	9.864168	1.183112
									0.04			1.453934	1.138534	9.535765	1.185900
										0		1.502201	1.175421	16.165724	1.174663
										0.5		1.502201	1.175421	12.537127	1.176193
0.1	0.1	1.0	1.0	0.1	1.0	1.0	1.0	0.01	0.01	**1**	1.0	1.502201	1.175421	10.548769	1.177527
										1.5		1.502201	1.175421	9.261890	1.178726
										2		1.502201	1.175421	8.346304	1.179825
											0	1.502201	1.175421	10.548770	0.066667
											0.25	1.502201	1.175421	10.548770	0.495824
0.1	0.1	1.0	1.0	0.1	1.0	1.0	1.0	0.01	0.01	1.0	**0.5**	1.502201	1.175421	10.548770	0.765584
											0.75	1.502201	1.175421	10.548770	0.985764
											1	1.502201	1.175421	10.548769	1.177527

5. Results and discussion

Figures 3–6 present the effect of the porosity parameter D on the velocity components, temperature distribution, and concentration profile of the hybrid Williamson nanofluid containing BNNTs and CdTe nanoparticles dispersed in the RT42 HC. The velocity components in the x- and y-directions decrease with the elevation of the porosity parameter value, as shown in Figures 3 and 4. Such behavior is attributed to the increase of resistance supported by the porous medium. The governing momentum equations contain the Darcy–Forchheimer drag forces, which physically characterizes the permeability of the porous structure. So, high values of D number give rise to reducing fluid motion. The increase in porous resistance results in dissipating the momentum of the hybrid nanofluid which in turn implies an inhibition in the velocity field and a reduction of the hydrodynamic boundary layer thickness. As a result, stronger friction is experienced by the fluid particles within the porous matrix, and therefore, both velocity components decay gradually with the increase in distance from the surface.

In contrast, Figures 5 and 6 reveal a slight increase in both the temperature and concentration profiles upon elevating values of the porosity parameter. As a result of reducing the fluid velocity, the convective transport of heat and nanoparticles become weaker within the boundary layer, which allows thermal energy and nanoparticle concentration to accumulate near the surface. Consequently, thinning of the thermal and concentration boundary layers occurs. The increased heat distribution can be linked to the thermophysical properties of the hybrid nanofluid. The boron nitride nanotubes (BNNTs) within the fluid exhibit high thermal radiation and excellent thermal stability, leading to a significant improvement in heat diffusion within the fluid. Simultaneously, the cadmium telluride (CdTe) nanoparticles provide additional semiconductor and optical properties, further enhancing energy absorption and thermal response. As a result of this synergistic interaction between these particles within the RT42 HC material, the overall heat transfer capacity of the hybrid nanofluid system is enhanced. The concentration profile in Figure 6 shows that the concentration increases, justified by the decrease of convective mass transport due to the resistance of excretion by the porous medium.

As the fluid velocity decreases, a reduction of the migration of nanoparticles away from the wall takes place. This, in turn, leads to greater accumulation of nanoparticles in the boundary layer region. Practically speaking, these results further demonstrate that permeability plays a crucial role in regulating momentum, heat, and mass transfer mechanisms in hybrid nanofluid systems. The significant decrease in velocity, accompanied by an increase in the thermal field and concentration, indicates that the porosity parameter is an effective control factor in thermal management applications. In particular, the hybrid nanofluid composed of BNNT, and CdTe nanoparticles dispersed in RT42 HC PCM proves high potential for electronic cooling systems and solar energy technologies, where efficient heat dissipation and thermal regulation are essential.

The Forchheimer number indicates the inertial resistance within the porous medium. It accounts for the nonlinear drag force. Its importance is clear at higher flow velocities. The velocity components, temperature distribution, and concentration profile of the hybrid Williamson nanofluid composed of BNNT, and CdTe nanoparticles suspended in the RT42 HC material are apparently affected by the Forchheimer number (Fr), as depicted in Figures 7–10. Figures 7 and 8 show that the elevation of Forchheimer number leads to an apparent reduction of velocity components in the $f'(\eta)$ and $h'(\eta)$. It is evident from Figures 7 and 8 that increasing the Forchheimer number results in a clear reduction in the (x)-direction velocity component $f'(\eta)$, as well as in the y-direction velocity component $h'(\eta)$. The Forchheimer parameter gives rise to an additional inertial resistance term that is essential at moderate and high Reynolds numbers. An increase in Fr results in a stronger nonlinear drag force acting on the fluid. Such un effect acts to suppress the motion of the hybrid nanofluid within the boundary layer. Consequently, a thinning of the boundary layer takes place due to the decrease in the momentum of the fluid particles. A direct response of this effect is clearly observed in both velocity components; the increase in Forchheimer number forces the velocity magnitude to diminish gradually.

In contrast, the increase in the Forchheimer number results in a slight increase in the temperature profile $\theta(\eta)$, as shown in Figure 9.

The decrease in fluid velocity reduces the convective heat transport away from the surface, which enhances the thermal energy within the boundary layer. Consequently, the thermal boundary layer becomes thicker.

Boron nitride nanotubes (BNNTs) are characterized by high thermal conductivity and excellent thermal stability, leading to a significant improvement in heat conduction within the fluid. Simultaneously, cadmium telluride (CdTe) nanoparticles possess additional semiconducting and optical properties that facilitate better energy absorption and heat transfer. This synergistic interaction between BNNTs and CdTe dispersed in the RT42 HC medium contributes to a more efficient thermal response within the liquid system. Therefore, these nanoparticles further enhance the thermal diffusion.

Similarly, it can be observed that the concentration distribution increases with increasing values of the Forchheimer number, as shown in Figure 10. The enhanced inertial resistance within the medium inhibits the convectional movement of nanoparticles away from the wall, keeping them for a longer period within the boundary layer region. Consequently, the nanoparticle concentration increases, and the thickness of the boundary concentration layer increases. This observed behavior confirms the strong correlation between the resistance of the porous medium and the mass transfer characteristics in hybrid nanofluid flows. In general, these results highlight the important role of the Forchheimer coefficient in regulating momentum, heat, and mass transfer in medium flows. Reducing the fluid velocity and improving the temperature and concentration distributions have the potential for effectively utilizing the inertial resistance within the porous structure to control heat transfer in advanced hybrid nanofluid systems.

Figures 11–14 depict how thermophysical and chemical parameters affect the temperature and concentration distributions of the hybrid Williamson nanofluid composed of BNNTs and CdTe nanoparticles dispersed in the RT42 HC.

Figure 11 illustrates that increasing the activation energy coefficient δ leads to an increase in concentration $\Omega(\eta)$. This can be explained physically as follows: the activation energy is known to be the energy threshold required for chemical reactions to occur. If the activation energy value increases, it leads to a decrease in the rate of the chemical reaction due to the increased energy required. This, in turn, reduces the consumption of nanoparticles through reaction mechanisms, leading to accumulation or allowing a larger quantity of nanoparticles to remain within the concentration boundary layer. This means an increase in concentration and an increase in the thickness of the concentration boundary layer.

Figure 12 demonstrates that higher values of the temperature difference parameter ε correspond to lower values of the concentration profile. The temperature difference factor ε is prominent in the Arrhenius reaction term and affects the reaction rate through the exponential dependence of the ε value on temperature. The higher the ε value, the more intensive the reaction process becomes. This, in turn, leads to a decrease in the concentration of nanoparticles within the fluid, resulting in a thinner mass boundary layer and a lower concentration.

The effect of the chemical reaction coefficient γ on concentration distribution $\Omega(\eta)$ is illustrated in Figure 13, where it is observed that the concentration distribution decreases with increasing values chemical reaction coefficient γ. Physically, with an increase in the chemical reaction coefficient, nanoparticles are consumed within the concentration boundary layer. The higher the value of this coefficient, the faster the depletion of nanoparticles in the liquid region. This, in turn, leads to a decrease in the concentration distribution and a thinning of the concentration boundary layer.

Figure 14 illustrates the influence of the Schmidt number Sc, which represents the ratio of momentum diffusivity to mass diffusivity, on the concentration distribution. The figure shows a significant reduction of the concentration profile as Sc increases. Physically, higher values of Sc corresponds to lower mass diffusivity. The decrease in the diffusion of nanoparticles results in weak ability of nanoparticles to spread within the fluid, which in turn leads to a thinner concentration boundary layer and a reduction in the concentration distribution.

Generally speaking, these results assure the crucial roles that thermal reaction parameters, activation energy, temperature difference, chemical reaction strength, and mass diffusivity play in optimizing the rates of heat and mass transfer in a hybrid nanofluid system. The inclusion of BNNTs and CdTe nanoparticles within the RT42 HC leads to enhanced thermal transport characteristics.

Figures 15–18 show how the velocity, temperature, and concentration profiles of the hybrid Williamson nanofluid using RT42 HC as the base vary upon changing the nanoparticle volume fractions φ_1 and φ_2, corresponding to CdTe and BNNTs nanoparticles.

Figures 15 and 16 show how the velocity components in the x- direction $f'(\eta)$ and in the y-direction $h'(\eta)$ vary with the nanoparticle volume fractions. It is observed that the increase in nanoparticle concentration results in a mild reduction in both velocity profiles throughout the boundary layer region. Physically, as additional nanoparticles are dispersed in the fluid, the effective viscosity and density of the hybrid nanofluid are increased, which elevates the internal resistance to fluid motion. As a result of increasing the nanoparticle volume fraction, the intermolecular interactions within the fluid become stronger, so the momentum resistance increases, which lowers the velocity field. Consequently, the hydrodynamic boundary layer thin as a result of the increasing concentration of nanoparticles.

Figure 17 shows the effect of nanoparticle size ratios on the temperature distribution $\theta(\eta)$. The figure shows that the temperature curve rises with increasing nanoparticle concentration. Physically, this resulting temperature increase is mainly due to the enhancement of effective thermal conductivity of the hybrid nanofluid. It is known that boron nitride nanotubes (BNNTs) have exceptional thermal conductivity and thermal stability, which explains the clear improvement in heat diffusion inside the fluid. In addition, cadmium telluride (CdTe) nanoparticles have semiconductor and optical properties that improve heat absorption and energy transfer.

Although higher nanoparticle fractions give rise to an increase in the effective thermal conductivity, the associated reduction in Nusselt number implies that the local wall heat-transfer rate is reduced under the present conditions. Therefore, the higher temperature profile is due to greater thermal-energy retention within the boundary layer.

Figure 18 depicts the influence of the nanoparticle volume fractions on the concentration profile $\theta(\eta)$. It is observed that the increase in the nanoparticle volume fraction reduces the concentration distribution. This behavior is due to the increase in effective viscosity of the hybrid nanofluid as a result of higher nanoparticle concentrations, so that the mass diffusion process becomes weaker within the boundary layer. Consequently, the mass transfer rate lowers, and the concentration boundary layer becomes thinner.

Overall, the results presented confirm that the inclusion of BNNTs and CdTe nanoparticles significantly influenced the heat transfer properties of the basic phase-change fluid, while the fluid velocity decreased slightly due to increased viscosity. The improvement in the system's thermal performance resulted from the increased thermal conductivity of the hybrid nanofluid.

The combined effect of the porosity parameter D and the Forchheimer number Fr on the coefficient of skin friction, written in terms of the velocity gradient $f''(0)$, is presented in Figure 19. It can be noticed that the surface expressing this relation is not flat, indicating that the wall shear stress is not regulated by a single resistance mechanism. In fact, it arises from the nonlinear inertial drag, and the linear Darcy drag within the porous medium structure. The sign of $f''(0)$ is negative since $f'(0)$ changes from 1 to 0. From the physical point of view, the absolute value of $f''(0)$ refers to the strength of the wall drag that acts in opposite direction to the stretching motion. The surface in Figure 19 shows that the wall shear increases with the increase in porous-medium resistance. This is physically justified by the porous matrix extracting momentum from the Williamson hybrid nanofluid. The fluid encounters greater resistance as both the Fr and D increase, and the velocity gradient near the wall becomes more pronounced. This results in greater shear stress, despite the reduced velocity distribution within the boundary layer. This behavior is consistent with two-dimensional velocity diagrams, where both velocity components decrease with the increase of porous resistance. The Forchheimer number Fr represents the interial resistance, so it has an essential role in the 3D surface. As the local fluid motion increases, the role of Fr becomes very important. The increase in Fr results in an additional nonlinear drag term. This drag reduces the momentum of the fluid particles and increases the effective resistance of the medium.

Figure 20 shows the three-dimensional variation in the Nusselt-number quantity $-\theta'(0)$, which represents the wall heat-transfer rate, with the nanoparticle volume fractions φ_1 and φ_2. Since the value of the Nusselt number is affected clearly by both φ_1 and φ_2, one concludes that the hybridization of CdTe and BNNTs has a direct influence on the heat-transfer behavior of the RT42 HC.

Taking into account the negative-sign convection of the Nusselt number, this behavior can be interpreted physically as follows: The BNNTs give rise to good thermal conduction paths and thermal stability alongside the contribution of the CdTe nanoparticles to additional semiconductor and optical absorption characteristics.

Figure 20 shows that the increase in any nanoparticle volume fraction results in decreasing the reduced Nusselt number. So, while effective thermal conductivity increases, the local heat-transfer rate from the stretching surface decreases. This can be attributed to changes in viscosity, heat capacity, temperature distribution, and thermal-boundary-layer thickness. So, it is important to optimize the composition of nanoparticles in order to get a cooling enhancement.

Figure 21 presents a contour map for the temperature field $\theta(\eta)$ as a function of the similarity variable η and the porosity parameter D. The contour distribution illustrates a simultaneous variation of θ in the normal direction, with porous-medium permeability enabling a better visualization than 2D plots of $\theta(\eta)$ with a single variable. This demonstrates the expected boundary layer behavior where the region near the stretching surface exhibits higher temperature followed by gradual decay toward the free stream.

The contour lines indicate that the parameter D influences the thickness and structure of the thermal layer. Increased porous resistance weakens the flow motion and reduces convection heat transfer from the surface. This results in thermal energy remaining within the boundary layer for a longer period, leading to an expansion of the high-temperature zone near the wall. This behavior was previously observed in the temperature phase associated with the Darcy number.

The density of the contour lines away from the wall indicates the region where the temperature drops rapidly towards the ambient temperature. In the context of RT42 HC fluid, this behavior is suitable, as the phase-change material stores heat within a limited temperature range. The nanoparticles BNNTs and CdTe inserted in the fluid distribute the absorbed heat, and the duration of heat retention is controlled by the porous medium. The combined role of thermal-storage and thermal-diffusion of the hybrid nanofluid is well described in the contour map.

Figure 21 suggests that the porous structure can be used as a control mechanism in practical cooling systems. The relevant value of the parameter D helps to keep a stable thermal layer preventing a sudden temperature rise in electronic devices. However, strong porous resistance implies a weak convective transport that may slow down the process of heat removal from the wall. Therefore, the optimal selection of the value of the parameter D must be done in conjunction with the selection of the nanoparticle volume fractions, and this leads to achieving safe temperature regulation and acceptable flow resistance.

To complement the one-dimensional similarity profiles, Figures 22–24 provide a two-dimensional visualization of the flow, thermal, and species-transport structures associated with the hybrid nanofluid. This aims to show the distribution of the considered boundary layer quantities in the physical x–z plane and how the effect of stretching surface damps far from the wall.

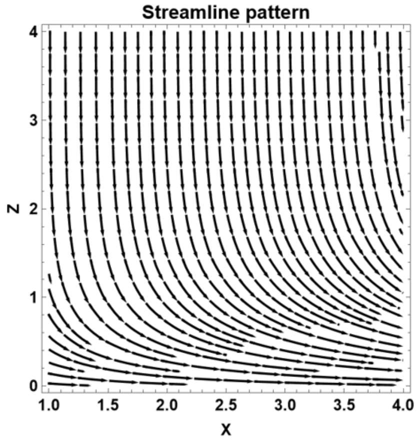

Figure 22. Streamline pattern in the physical x, z plane.

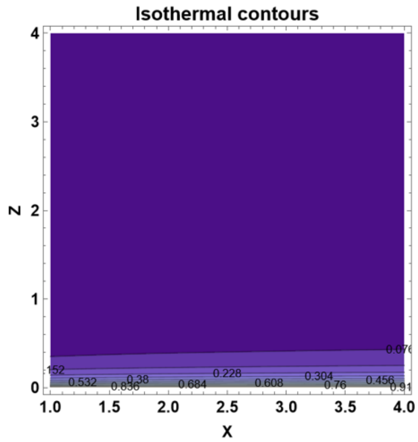

Figure 23. Isothermal contours of the dimensionless temperature in the physical x,z plane.

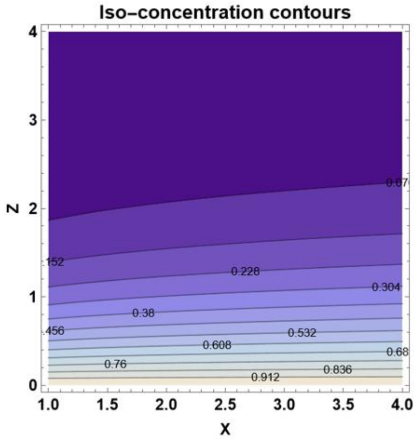

Figure 24. Iso-concentration contours of the dimensionless concentration in the physical x,z plane.

The streamline pattern in the x-z plane is displayed in Figure 22. For small values of z, which indicate the region close to the surface, the curvature of the streamlines is high, while the streamlines become almost vertical as z increases. This trend is due to the fact that the effect of stretching motion is higher near the wall, where the fluid is entrained and redirected within the boundary layer. The smoothness of the streamlines refers to the stability of the boundary layer structure for the selected parameter values. The direction of the streamline undergoes greater change near the lower part of the domain, confirming that the main momentum adjustment takes place near the wall.

Figure 23 presents the isothermal contours. The contours seem to be very crowded in a small region adjacent to the surface. Uniform low-temperature levels are observed clearly in most of the outer domain. The density of the contours near the wall refers to the large temperature gradient in the normal direction, providing a clue that the thermal boundary layer is thin. Getting apart from the surface, with the increase of z, a wide separation between the contours is observed, which enforces a rapid approximation of temperature to the ambient conditions.

In contrast to the isothermal contours, the iso-concentration contours of the dilute reactive species, shown in Figure 24, are extended over a large distance in the z-direction. As z increases, the concentration decreases progressively until it reaches its free-stream value, resulting in a concentration boundary layer thicker than the thermal layer for the same parameter values. The contour bands are almost horizontal, which refers to the normality of the concentration gradient to the surface. The slight variation of the contour bands along the x axis refers to the combined effect of streamwise convection, molecular diffusion, and the Arrhenius-type chemical reaction. The contours spread gradually away from the wall, which implies that the reactive species are more noticeable in the fluid than the thermal disturbance.

Figures 8, 10, 12, and 15–18 show small separations between the profiles, since the parameter range used is designed to maintain physically realistic conditions and numerical regularity. The enlarged insets are included to show the differences between profiles, keeping the parameter real-valued range.

Engineering applications can benefit from the results obtained in this work, which assure the essential roles of the controlling parameters in balancing thermal regulation, flow resistance, and species transport in cooling and reactive flow systems. The linear and nonlinear resistances of the porous medium are enhanced upon increasing the inverse of the porosity parameter D number and Forchheimer number, respectively. That increase in resistance reduces the fluid velocity and expands the residence time of heat and reactive species near the surface, leading to improved temperature uniformity in electronic-cooling channels. However, such increased resistance enhances wall shear, pumping-power requirements, and the time needed to cool the heated surface. The increase in volume fractions of the CdTe and BNNT nanoparticles refines the thermal storage and heat spreading within the base fluid, since the effective thermal conductivity rises. Nevertheless, the viscous resistance also increases, and the reduced Nusselt number decreases as a result of reducing the wall-temperature gradient. So, an optimized nanoparticle composition leads to a balance between temperature uniformity, frictional losses, and surface heat removal. It may be beneficial for solar-thermal and thermal-energy-storage systems to raise the thermal radiation and viscous dissipation since they imply the enhancement of fluid temperature and promote heat retention. However, this also has an inverse effect on the efficiency of heat extraction at the wall. The chemical reaction, activation energy, temperature-difference, and Schmidt-number parameters are essential parameters to control the mass diffusion and species consumption. So, applications including chemical-reaction systems, catalytic surfaces, and reactive cooling fluids can benefit from optimizing the values of such parameters. Therefore, the optimization of controlling parameters should depend on whether the desired design aims to enhance rapid wall cooling, reduced pumping power, controlled mass transfer, or uniform heat distribution.

Table 3 summarizes the effect of the governing parameters on the positive magnitude of the wall gradients $-f''(0)$, $-h''(0)$,$-\theta'(0)$, and $-\Omega'(0)$. The effects of the thermal reaction parameters A and B are clear on the heat-transfer and mass-transfer quantities. As A increases from 0.1 to 2, the heat transfer quantity $-\theta'(0)$ decreases from 10.548769 to 10.361025, and $-\Omega'(0)$ increases slightly from 1.177527 to 1.178191. A similar but weaker behavior is observed for B. So, A and B act mainly on thermal control parameters and have almost no effect on the momentum control parameters. Physically, as the thermal reaction contribution increases, the thermal activity inside the boundary layer rises, which results in a reduction of the wall temperature gradient, corresponding to lower values of the Nusselt number. Engineering applications can benefit from varying A and B to control the thermal response of the BNNTs+CdTe/RT42 HC hybrid PCM nanofluid, while the wall drag is not significantly affected.

The Darcy number has a considerable effect on all the values of $-f''(0)$, $-h''(0)$,$-\theta'(0)$, and $-\Omega'(0)$. Values in Table 3 show that, as D increases from 0.4 to 2, $-f''(0)$ increases from 1.379686 to 1.678644, and $-h''(0)$ increases from 1.073901 to 1.320487. Therefore, the skin friction rises in both stretching directions. As the skin friction rises, the porous resistance enhances the velocity gradient at the wall and, consequently, the mechanical interaction between the hybrid nanofluid and the surface becomes stronger. Against this behavior is the behavior of $-\theta'(0)$ and $-\Omega'(0)$, since for the same variance of D, $-\theta'(0)$ drops from 11.610495 to 8.892590 and $-\Omega'(0)$ drops from 1.194647 to nearly 1.154469. So, the increase of D in this formulation results in weakening the heat and mass transfer. The physical interpretation of this is that as the porous medium resistance increases, the convective transport decreases, allowing thermal energy and inserted nanoparticles to remain longer in the boundary layer. For engineering applications, such as porous heat sinks and electronic cooling systems, it is an optimization problem to have a design following this trend: although the increase of porous resistance gives rise to the enhancement of residence time and thermal storage, it also causes a frictional loss and a reduction of local wall-heat extraction rate.

The activation-energy parameter δ is coupled with the species equation so that the only number affected by changing δ in Table 3 is $-\Omega'(0)$. Upon increasing δ from 0 to 2, $-\Omega'(0)$ decreases from 1.462944 to 1.025586, while the values of $-f''(0)$, $-h''(0)$,$-\theta'(0)$ remain unchanged at 1.006329, 0.405597, and 9.038130, respectively. The increase in δ results in weaking the concentration at the wall, which implies lower values than the Sherwood number. This result may help in practical applications since the surface geometry or wall-thickness variation may help to regulate nanoparticle deposition and mass-transfer intensity while the momentum and thermal fields remain undisturbed.

The heat-transfer rate is reduced primarily by the Eckert number Ec as shown in Table 3. As Ec increases from 0 to 0.4, the value of $-\theta'(0)$ drops sharply from 11.610495 to 2.496107, while the values of $-f''(0)$ and $-h''(0)$ do not change. Such a large decrease of the wall temperature gradient is due to viscous dissipation. The larger the value of Ec, the more kinetic energy is converted into thermal energy, which leads to raising the temperature inside the boundary layer and lowering the temperature difference between the surface and the adjacent fluid. Consequently, the local Nusselt number decreases. Changing the Eckert number from 0 to 0.2 has no big effect on the values of $-\Omega'(0)$, as shown in Table 3, related to a weak coupling between viscous heating and the concentration field. This result is very important in high-heat-flux electronic devices, since as viscous dissipation increases the net cooling ability of the working fluid is reduced even when the nanofluid has enhanced thermal conductivity. The temperature difference parameter ε mainly influences the rate of mass transfer.

Increasing the temperature-difference parameter ε from 0.5 to 4 leaves the momentum and heat-transfer quantities unchanged but increases $-\Omega'(0)$ from 1.050414 to 1.099540. This shows that ε intensifies the concentration gradient at the surface.

Since ε appears in the contribution of the Arrhenius reaction, the increase of ε implies a modification in the reaction's sensitivity to temperature, accelerating the consumption of chemical species near the wall, thus thinning the concentration layer at the limiting concentration and increasing the Sherwood number. This trend is useful in applications dependent on controlling the rate of species transport, such as surface coating processes.

The increase of the Forchheimer number Fr leads to an increase in the magnitude of the wall shear. As Fr increases from 0 to 2, $-f''(0)$ increases from 0.717499 to 1.221214. Fr has also a considerable but smaller effect on the values of $-h''(0)$. This proves that the nonlinear inertial resistance associated with the Forchheimer term enhances wall drag and lowers the fluid motion inside the porous matrix. The value of $-\theta'(0)$, which refers to the heat-transfer rate, decreases from 9.832340 to 8.279224, indicating that as the inertial resistance increases, the wall thermal gradient decreases through weakening convective heat removal. Generally, the change of Fr does not lead to a big change in the mass-transfer quantity. Consequently, Fr primarily acts through the momentum field and has indirect effects on both heat and species transfer. The value of Fr should be optimized for applications such as porous electronic cooling channels, since the increase of Fr improves residence time but also leads to an increase in pumping power requirements.

The mass transfer is directly affected by the chemical reaction parameter γ, as shown in Table 3. Upon increasing γ from 0 to 2, the value of $-\Omega'(0)$ increases from 0.822839 to 1.239028, while both the skin friction and heat-transfer remain unchanged. As a result of this increase in Sherwood number, the chemical reaction sharply lowers the concentration gradient at the wall. From the physical point of view, as the chemical reaction increases, the rate of consuming the diffusion species inside the boundary layer increases strongly, leading to a decrease in the concentration away from the wall and producing a thinner concentration boundary layer. What is important about this finding, besides its consistency with concentration-profile results, is its relevance to the transport of chemically reactive nanofluids, controlled nanoparticle deposition, and catalytic surfaces.

The nanoparticle volume fractions φ_1 and φ_2 affect both mechanical and thermal behavior. $-f''(0)$ increased from 1.484020 to 1.547757, and $-h''(0)$ increased also from 1.161523 to 1.210267 upon increasing φ_1 from 0 to 0.04. But the increase of φ_2 from 0 to 0.04 results in decreasing $-f''(0)$ from 1.518643 to 1.453934 and increasing $h''(0)$ from 1.187994 to 1.138534. Meanwhile, the reduced Nusselt number $-\theta'(0)$ decreases with the increase of φ_1 and φ_2: it decreases from 11.076745 to

9.068670 for φ_1 and from 10.906175 to 9.535765 for φ_2. Although this finding may appear as the nanofluid becoming thermally inefficient, in fact, it indicates that the temperature inside the boundary layer becomes higher and more uniformly distributed, because the BNNTs+CdTe/RT42 HC suspension improves thermal conduction and thermal storage. As the temperature gradient decreases the thermal boundary layer becomes thicker. Therefore, high nanoparticle fraction improves bulk heat spreading and thermal regulation, but it also increases wall drag and may reduce the local Nusselt number. This is a key engineering trade-off in designing PCM-based nanofluid coolants.

The radiation parameter Rd has a strong effect on reduced Nusselt number $-\theta'(0)$. As Rd increases from 0 to 2, $-\theta'(0)$ sharply decreases from 16.165724 to 8.346304, while the two skin-friction quantities remain unchanged. In fact, the thermal radiation parameter is coupled with the energy equation. As the thermal radiation gets higher, the radiative heat contribution inside the boundary layer increases and the fluid temperature elevates, hence a reduction of the wall temperature gradient takes place. The mass-transfer quantity is weakly affected; it only increases from 1.174663 to 1.179825. In engineering applications such as solar systems and high-temperature electronic cooling applications, an important role of thermal radiation is to redistribute heat within the working fluid but a reduction of the efficiency of heat extraction at the heated surface may take place due to excessive radiative heating.

The Schmidt number Sc majorly influences the mass-transfer parameter. The increase of Sc from 0 to 1 results in an increase of the value of $-\Omega'(0)$ from 0.066667 to 1.177527, whereas the momentum and heat-transfer quantities practically do not change. The parameter Sc is the ratio of momentum diffusivity to mass diffusivity, so higher values of Sc correspond to lower species diffusivity. Consequently, an increase in Sc results in thinning the concentration boundary layer and a greater magnitude of the concentration gradient at the wall, implying a larger Sherwood number. Such behavior is fully consistent with the results in Figure 14, which presents the concentration profile with varying Sc.

6. Concluding remarks

This study numerically investigated the transport characteristics of a three-dimensional Williamson hybrid nanofluid containing BNNTs and CdTe nanoparticles dispersed in RT42 HC, which is considered in its fully molten state, over a nonlinear stretching surface embedded in a Darcy, Forchheimer porous medium. The principal findings are summarized as follows:

- The porosity parameter D and Forchheimer parameters significantly suppress the fluid velocity while enhancing the thermal and concentration fields, demonstrating the strong influence of porous medium resistance on transport processes.
- Thermal reaction parameters, thermal radiation, and viscous dissipation increase the fluid temperature and thicken the thermal boundary layer, whereas activation energy enhances the concentration field by suppressing the chemical reaction.
- Increasing the chemical reaction parameter, temperature difference parameter, and Schmidt number reduces the concentration boundary layer due to accelerated reactive-species consumption and reduced mass diffusivity.
- Increasing the volume fractions of CdTe and BNNT nanoparticles improves the thermal performance of the hybrid nanofluid despite a slight reduction in fluid velocity caused by the increase in effective viscosity.
- The governing parameters provide effective control over the skin friction coefficients, heat transfer, and mass transfer characteristics, offering flexibility in optimizing the transport behavior of the hybrid nanofluid for practical thermal applications.

Nomenclatures.

$x, y, z\ (m)$	Cartesian coordinate along the x, y, z direction
$u, v, w(m/s$	Velocity component in the x, y, z −direction
T	Temperature (K)
t	Time (s)
V	Flow rate volume
U_0, V_0	Characteristic velocities
Q^*	Heat generation/absorption coefficient
T_0	Characteristic temperature
C_p	Heat capacitance
$C_F(-)$	Inertial coefficient
C	Fluid concentration
V	Fluid velocity
$k(W/mK)$	Thermal conductivity
n	Power index parameter
$q_r(W/m^2)$	Radiative heat flux
C_{fx}	Local skin friction coefficient
Nu_x	Local Nusselt number
Greek symbols	
θ	Dimensionless temperature
ϕ	Nanoparticles concentration
φ	Nanoparticles volume fraction
$\rho(kg/m^3)$	Fluid density
$\mu(Ns/m^2)$	Dynamic viscosity
$\nu(m^2/s)$	Kinematic viscosity
Γ	Time constant
α	Stretchable ratio parameter
Dimensionless parameters	
Rd	Thermal radiation parameter
W_e	Weissenberg number
Ec	Eckert number
Pr	Prandtl number
Sc	Schmidt number
λ	Wall thickness variable
Re_x	Local Reynolds number
n	Velocity power index
Subscripts	
w	Quantities at surface
∞	Quantities far away from the surface
hnf	Hybrid nanofluid

Author contributions

Mohammed H Alharbi: Data curation, Investigation, Resources, Funding, Conceptualization, Writing–original draft, Writing–review & editing; Essam M. Elsaid: Formal analysis, Visualization, Investigation, Project administration, Methodology, Writing–original draft, Writing–review & editing; Tarek G. Emam: Conceptualization, Supervision, Methodology, Software, Validation, Writing–original draft, Writing–review & editing. All authors have read and agreed to the published version of the manuscript.

Use of Generative-AI tools declaration

The authors declare they have used Artificial Intelligence (AI) tools in the creation of this article.

Acknowledgments

This work was funded by the University of Jeddah, Jeddah, Saudi Arabia, under grant No. (UJ-25-DR-711). Therefore, the authors thank the University of Jeddah for its technical and financial support.

Conflict of interest

The authors declare there is no conflict of interest.

References

1. B. N. Lakshmi, C. Maheswari, V. S. Bhagavan, S. L. Pala, A. Anjum, U. Khan, et al., Numerical investigation of velocity and thermal slips on MHD hybrid nanofluid flow past a stretching sheet with nth-order chemical reaction effects, *Eng. Rep.*, **8** (2026), e70760. https://doi.org/10.1002/eng2.70760
2. S. A. Qureshi, A. Qureshi, S. Shoaib, Numerical treatment of the magnetised dissipative thin-film hybrid nanofluid (S WCNT− MWCNT/H_2O) flow and heat transfer over an unsteady stretching sheet with partial slip and convective boundary conditions, *Int. J. Ambient Energy*, **47** (2026), 2660869. https://doi.org/10.1080/01430750.2026.2660869
3. N. H. A. Norzawary, N. Bachok, M. S. Mustafa, S. K. Soid, Velocity and thermal slip of hybrid carbon nanotubes via extendable/shrinkable cylinder: Heat transfer optimization, *Z. Angew. Math. Mech.*, **106** (2026), 70399. https://doi.org/10.1002/zamm.70399
4. E. O. Fatunmbi, A. T. Adeosun, S. O. Salawu, O. A. Olaiju, Thermal efficiency of MHD micropolar penta-hybrid nanofluid squeezing flow under nonlinear thermal radiation and activation energy effects, *Int. J. Thermofluids*, **33** (2026), 101626. https://doi.org/10.1016/j.ijft.2026.101626
5. N. S. Akbar, T. Zamir, T. Muhammad, M. Farooq, N. Ullah, S. Shukat, Thermal performance with neural network analysis of Maxwell fluid with hybrid and tri-nanoparticle interactions: A case study, *Neural Comput. Applic.*, **38** (2026), 322. https://doi.org/10.1007/s00521-026-11996-2

6. D. A. Kanwal, I. B. Mansir, N. A. Alshehri, Z. Zheng, D. Qaiser, M. A. Fahmy, et al., Heat and mass transfer analysis for bi-dimensional bioconvective MHD nanofluid with varying thermal traits, *Int. J. Model. Simul.*, **46** (2026), 693–707. https://doi.org/10.1080/02286203.2024.2349505
7. A. Mishra, Significance of Thompson and Troian slip effects on Fe3O4-CoFe2O4 ethylene glycol-water hybrid nanofluid flow over a permeable plate, *Hybrid Adv.*, **6** (2024), 100262. https://doi.org/10.1016/j.hybadv.2024.100262
8. A. Mishra, G. Pathak, Thermal-flow characteristics of an Ellis hybrid nanofluid containing polytetrafluoroethylene-SWCNTs over a stretching/shrinking cylinder with slip effect, *Nano-Structures Nano-Objects*, **43** (2025), 101515. https://doi.org/10.1016/j.nanoso.2025.101515
9. A. U. Awan, S. Majeed, B. Ali, L. Ali, Significance of nanoparticles aggregation and Coriolis force on the dynamics of Prandtl nanofluid: The case of rotating flow, *Chin. J. Phys.*, **79** (2022), 264–274. https://doi.org/10.1016/j.cjph.2022.07.008
10. S. Kanwal, S. A. A. Shah, A. Bariq, B. Ali, A. E. Ragab, E. A. Az-Zo'bi, Insight into the dynamics of heat and mass transfer in nanofluid flow with linear/nonlinear mixed convection, thermal radiation, and activation energy effects over the rotating disk, *Sci. Reports*, **13** (2023), 23031. https://doi.org/10.1038/s41598-023-49988-0
11. A. Ali, H. Sharif, D. Habib, H. A. Ghazwani, I. Saman, H. Yang, Significance of tri-hybrid nanoparticles in thermal management subject to magnetized squeezing flow of a Boger-micropolar nanofluid between concentring disks, *J. Mol. Liq.*, **397** (2024), 124141. https://doi.org/10.1016/j.molliq.2024.124141
12. L. Ali, M. G. Murtaza, T. Akter, J. Alam, The effect of electrical conductivity and magnetization on biomagnetic fluid flow containing magnetic particles past a thin needle using lie group analysis, *J. Therm. Anal. Calorim.*, **151** (2026), 9245–9259. https://doi.org/10.1007/s10973-026-15493-5
13. Z. Said, A. K. Pandey, A. K. Tiwari, B. Kalidasan, F. Jamil, A. K. Thakur, et al., Nano-enhanced phase change materials Fundamentals and applications, *PECS*, **104** (2024), 101162. https://doi.org/10.1016/j.pecs.2024.101162
14. S. Chang, X. Li, X. Gao, R. Lin, H. Hu, Y. Shu, Numerical investigation on the heat transfer characteristics and dynamic adaptability of cascaded phase change material (PCM) heat sinks under flight conditions, *Energy*, **345** (2026), 140206. https://doi.org/10.1016/j.energy.2026.140206
15. S. D. Prasetyo, Y. Trisnoaji, Z. Arifin, A. R. Prabowo, Assessment of the performance differences in PV–PCM systems with numerical analysis of different phase change materials and structural designs, *Solar Energy Mater. Solar Cells*, **295** (2026), 114019. https://doi.org/10.1016/j.solmat.2025.114019
16. D. S. Jayathunga, H. P. Karunathilake, M. Narayana, S. Witharana, Phase change material (PCM) candidates for latent heat thermal energy storage (LHTES) in concentrated solar power (CSP) based thermal applications-a review, *Renew. Sust. Energy Rev.*, **189** (2024), 113904. https://doi.org/10.1016/j.rser.2023.113904
17. S. Kasiviswanathan, M. I. Shajahan, R. Bharathiraja, M. Arunprasad, A. C. Benime, Comprehensive overview of phase change materials in electronics, building, and solar applications, *Eng. Res. Express*, **8** (2026), 032502. https://doi.org/10.1088/2631-8695/ae342a
18. M. K. Saudi, M. Emam, H. Hassan, H. Sekiguchi, A. S. G. Khalil, Enhancing thermal management of lithium-ion batteries using phase change materials and expanded graphite: An experimental study, *J. Energy Storage*, **130** (2025), 117427. https://doi.org/10.1016/j.est.2025.117427

19. R. A. Rachmanto, Z. Arifin, Ubaidillah, W. Endra Juwana, E. Yohana, D. Widhiyanuriyawan, et al., Enhancing thermal performance and energy efficiency in photovoltaic thermal-phase change material systems: a numerical investigation of fin geometry variations, *Int. J. Heat Technol.*, **44** (2026), 201–214. https://doi.org/10.18280/ijht.440117
20. I. I. Hakim, R. Edriawan, N. Putra, Thermal performance and properties analysis of a building envelope integrated with phase change material for energy conservation in a tropical climate region, *AIP Conf. Proc.*, **2836** (2024), 080003. https://doi.org/10.1063/5.0188417
21. A. Srinu, K. S. Reddy, N. Amar, Radiation and inclined magnetic field effects on Williamson fluid flow above a stretching sheet in the existence of velocity, thermal, and concentration slips, *PDE Appl. Math.*, **9** (2024), 100611. https://doi.org/10.1016/j.padiff.2023.100611
22. S. T. Abbas, I. H. Qureshi, M. Sohail, M. J. Khan, Numerical investigation of williamson nanofluid heat transfer over a stretching sheet employing buongiorno model and bvp4c boundary layer solution, *PDE Appl. Math.*, **18** (2026), 101362. https://doi.org/10.1016/j.padiff.2026.101362
23. B. G. Negash, H. Dessie, E. Haile, T. Walelign, Magnetohydrodynamic analysis of unsteady williamson nanofluid flow over a permeable inclined stretching sheet with cattaneo-christov double-diffusion effects, preprint paper, 2026. https://doi.org/10.21203/rs.3.rs-9411000/v1
24. R. A. Oderinu, T. A. Oyeyinka, S. Alao, F. J. Ayanbukola, B. A. Sanusi, Mixed convection and permeability effects on magnetohydrodynamic williamson fluid flow over an inclined stretchy surface with radiation influence, *Eng. Rep.*, **7** (2025), e70078. https://doi.org/10.1002/eng2.70078
25. P. Priyadharshini, V. Karpagam, P. Gayathri, Numerical and ANN optimization analysis for Williamson fluid flow across a porous surface, *Neural Comput. Appl.*, **38** (2026), 333. https://doi.org/10.1007/s00521-026-12073-4
26. M. Madhu, N. S. Shashikumar, K. Thriveni, B. J. Gireesha, B. Mahanthesh, Irreversibility analysis of the MHD Williamson fluid flow through a microchannel with thermal radiation, *Waves Random Compl. Med.*, **35** (2025), 10105–10127. https://doi.org/10.1080/17455030.2022.2111473
27. M. Hasnain, H. Sezer, J. H. Mason, Mathematical modeling of heat and mass transfer in metal hydride hydrogen storage systems: A comprehensive review, *Renew. Sust. Energy Rev.*, **226** (2026), 116294. https://doi.org/10.1016/j.rser.2025.116294
28. Y. Jin, X. Yang, Q. Zeng, H. Deng, X. Gao, H. Xu, Research on heat and mass transfer of PEMEC anode flow channel based on topology optimization, *Fuel*, **404** (2026), 136144. https://doi.org/10.1016/j.fuel.2025.136144
29. K. Zhang, D. Yang, L. Wang, C. Gu, K. Wang, Macro-micro simulation of heat and mass transfer, grain growth during ultrasonic vibration-assisted wire-arc directed energy deposition, *Int. J. Heat Mass Transfer*, **256** (2026), 128038. https://doi.org/10.1016/j.ijheatmasstransfer.2025.128038
30. M. Sharifi, Effects of various instabilities on heat and mass transfer characteristics and their analysis in practical multidiffusive flow systems: A comprehensive review, *Int. Commun. Heat Mass Transfer*, **162** (2025), 108685. https://doi.org/10.1016/j.icheatmasstransfer.2025.108685
31. A. Atia, S. Benarrache, H. M. Regue, M. Teggar, S. Bouabdallah, N. H. Hamza, et al., Heat and mass transfer enhancement with latent heat thermal storage for improving the solar still performance: A comprehensive review, *Appl. Therm. Eng.*, **279** (2025), 128061. https://doi.org/10.1016/j.applthermaleng.2025.128061
32. M. A. Fahmy, A new boundary element formulation for modeling and simulation of three-temperature distributions in carbon nanotube fiber reinforced composites with inclusions, *Math. Meth. Appl. Sci.*, **49** (2026), 7550–7565. https://doi.org/10.1002/mma.7312

33. M. A. Fahmy, M. Toujani, A. E. Abouelregal, A boundary element framework for fractional dual-phase-lag modeling of nanoparticle-assisted photothermal heat transfer in skin tissue, *Results Eng.*, **29** (2026), 109417. https://doi.org/10.1016/j.rineng.2026.109417
34. J. H. Merkin, N. C. Roșca, A. V. Roșca, I. Pop, MHD mixed convection flow over a permeable vertical flat plate embedded in a Darcy–Forchheimer porous medium, *Transp. Porous Med.*, **1511** (2024), 2511–2528. https://doi.org/10.1007/s11242-024-02124-6
35. H. C. Nagari, M. D. Firdi, E. H. Rikitu, Investigation of thermal radiation and joule heating effects on variable viscosity Casson nanofluid flow over a stretching sheet in Darcy–Forchheimer porous medium, *Numer. Heat Transfer Part A*, **87** (2026), 2382929. https://doi.org/10.1080/10407782.2024.2382929
36. Q. Raza, X. Wang, Analyzing heat transfer behavior in two-dimensional Darcy–Forchheimer porous medium using magnetized nanoparticles, *Numer. Heat Transfer Part B*, **86** (2025), 4314–4334. https://doi.org/10.1080/10407790.2024.2380034
37. Q. Raza, X. Wang, A. J. Chamkha, Bio-convection of ternary magnetized nanoparticles thermal conductivity in chemical reaction and activation energy flow with Darcy Forchheimer permeable across a double porous medium, *Numer. Heat Transfer Part A*, **87** (2026), 2316210. https://doi.org/10.1080/10407782.2024.2316210
38. S. N. Safiullah, P. De, Thermal radiation, heat generation/absorption effect on bioconvective Sisko nanofluids over Darcy Forchheimer porous medium with regression analysis, *Numer. Heat Transfer Part B.*, **87** (2026), 2390099. https://doi.org/10.1080/10407790.2024.2390099
39. L. Ahmad, S. Islam, A. M. Alqahtani, M. Sarfraz, Swirling motion of temperature-dependent chemical reactions and Arrhenius activation energy in Cross fluid, *Int. Commun. Heat Mass Transfer*, **159** (2024), 108082. https://doi.org/10.1016/j.icheatmasstransfer.2024.108082
40. T. Muhammad, F. Haider, Time-dependent flow of Reiner–Rivlin nanofluid over a stretching sheet with Arrhenius activation energy and binary chemical reaction, *Multidiscip. Model. Mater. Struct.*, **21** (2025), 1–18. https://doi.org/10.1108/MMMS-05-2024-0123
41. M.I.U. Rehman, H. Chen, F. Z. Duraihem, M. Hussien, A. Hamid, H. Qi, Darcy-Forchheimer aspect on unsteady bioconvection flow of Reiner-Philippoff nanofluid along a wedge with swimming microorganisms and Arrhenius activation energy, *Numer. Heat Transfer Part A*, **87** (2026), 2314221. https://doi.org/10.1080/10407782.2024.2314221
42. M. M. Ghazy, Kh. S. Mekheimer, A. M. Megahed, R. E. Aboelkhair, Iirreversibility and controlled entropy generation for squeezing sutterby nanofluid flow with joule heating and arrhenius activation energy, *Z. Angew. Math. Mech.*, **106** (2026), e70412. https://doi.org/10.1002/zamm.70412
43. A. K. Gautam, A. K. Verma, K. Bhattacharyya, S. Mukhopadhyay, A. J. Chamkha, Impacts of activation energy and binary chemical reaction on MHD flow of Williamson nanofluid in Darcy–Forchheimer porous medium: A case of expanding sheet of variable thickness, *Waves Random Compl Med.*, **34** (2021), 3528–3549. https://doi.org/10.1080/17455030.2021.1979274
44. M. Taj, T. Salahuddin, A three dimensional frictional flow study of Williamson fluid with chemical reaction, *Mater. Sci. Eng.: B*, **291** (2023), 116305. https://doi.org/10.1016/j.mseb.2023.116305
45. M. Taj, T. Salahuddin, A brief flow analysis of Williamson fluid near a radiated irregular vertical surface with binary chemical reaction, *Waves Random Compl. Med.*, **36** (2026), 3604–3618. https://doi.org/10.1080/17455030.2023.2178835
46. S. M. R. S. Naqvi, H. Waqas, S. Yasmin, D. Liu, T. Muhammad, S. M. Eldin, et al., Numerical simulations of hybrid nanofluid flow with thermal radiation and entropy generation effects, *Case Stud. Therm. Eng.*, **40** (2022), 102479. https://doi.org/10.1016/j.csite.2022.102479

47. Z. Qin, C. Ji, Z. Low, S. Dubey, F. H. Choo, F. Duan, Effect of fin location on the latent heat storage: A numerical study, *Energy Proced.*, **143** (2017), 320–326. https://doi.org/10.1016/j.egypro.2017.12.691
48. P. N. S. Teja, S. K. Gugulothu, P. D. S. Reddy, A. Ashraf, B. Deepanraj, P. T. Arasu, Numerical study on the thermal enhancement of phase change material with the addition of nanoparticles and changing the orientation of the enclosure, *J. Nanomater.*, **2022** (2022), 6428469. https://doi.org/10.1155/2022/6428469
49. E. M. Elsaid, M. S. Abdel-Wahed, Thermal evaluation of MHD boundary-layer flow of hybridity nanofluid via a 3D sinusoidal cylinder, *Z. Angew. Math. Mech.*, **104** (2024), e202300186. https://doi.org/10.1002/zamm.202300186
50. T. Hayat, A. Aziz, T. Muhammad, A. Alsaedi, On magnetohydrodynamic three-dimensional flow of nanofluid over a convectively heated nonlinear stretching surface, *Int. J. Heat Mass Transfer*, **100** (2016), 566–572. https://doi.org/10.1016/j.ijheatmasstransfer.2016.04.113
51. A. A. Al Qarni, E. M. Elsaid, M. R. Eid, A. H. Abdel-Aty, A. J. Alqarni, M. S. Abdel-wahed, Heat transfer evaluation of (CaTe+SiC) hybrid nanofluid flow based RT42 HC (Rubitherm) phase change material: Cooling photovoltaic panels application, *Modern Phys. Lett. B*, **39** (2025), 2450440. https://doi.org/10.1142/S0217984924504402